ORIGINAL PAPER

Idealized simulations of the diurnal variation within the tropical cyclone boundary layer

Gabriel J. Williams Jr.[1]

Abstract

Recent numerical and observational studies have demonstrated that tropical cyclones undergo diurnal and semi-diurnal variability in precipitation rate and in its kinematic structure. However, the physical processes and mechanisms that govern the diurnal variability within the tropical cyclone boundary layer has not yet been examined. Numerical experiments using a high-resolution, non-hydrostatic, axisymmetric model are performed to examine the diurnal changes in the kinematic and thermal structure of the tropical cyclone boundary layer. It is shown that the numerical model used in this study reproduces the diurnal variability in the tropical cyclone boundary layer from previous observational studies. Using cross-correlation analysis, it is shown that enhanced radial inflow during the evening drives enhanced convection within the tropical cyclone boundary layer. Using budget analysis of potential temperature, water vapor mixing ratio, and radial inflow, it is shown that the combined effects of cloud evaporative cooling and nocturnal longwave radiative cooling destabilizes the outer regions of the tropical cyclone, and the net effect of this cooling is to initiate an overturning transverse circulation that enhances radial inflow during the evening hours. Conversely, the differential radiation pattern created by clouds in the outer core of the tropical cyclone boundary layer during the evening is reversed during the daytime by shortwave heating, which suppresses the overturning transverse circulation. The analysis suggests the diurnal changes in both lapse rate and cloudy-clear differential radiative heating are vital to the diurnal variation of the outer regions of the tropical cyclone boundary layer.

1 Introduction

The diurnal variation of precipitation and convection over the tropical oceans has been documented by numerous studies (e.g., Browner et al. 1977; Gray and Jacobson 1977; Randall et al. 1991; Mapes and Houze 1993; Liu and Moncrieff 1998; Yang and Slingo 2001; Ruppert and Hohenegger 2018). These studies have shown that cloud-top nocturnal radiative cooling and daytime radiative warming are important for promoting diurnal and semi-diurnal variations in tropical oceanic precipitation. Similarly, recent observational studies have suggested that tropical cyclone (TC) structure, especially the upper-level cirrus canopy clouds as measured by satellite infrared brightness temperatures, tends to vary following a diurnal cycle and/or semi-diurnal

cycle (e.g., Weickmann et al. 1977; Muramatsu 1983; Kossin 2002; Dunion et al. 2014; Bowman and Fowler 2015; Leppert and Cecil 2016; Wu and Ruan 2016; Ditchek et al. 2019a, b; Knaff et al. 2019).

The most comprehensive observational study on the tropical cyclone diurnal cycle (TCDC) was conducted by Dunion et al. (2014). This study found cyclical pulses (known as diurnal pulses) in the cirrus canopy of mature TCs (as seen by infrared satellite imagery) that propagate radially outward at a speed of 5–10 m s⁻¹. Similar to the Intertropical Convergence Zone (Ciesielski et al. 2018), these diurnal pulses begin forming near the time of sunset each day, and they appear as a region of cooling cloud-top temperatures. The pulse propagates radially outwards overnight to a radial distance of several hundred kilometers from the storm center by the following afternoon. Analyses of a 10 year dataset of storm-centered infrared satellite images suggested that the TCDC may be tied to TC dynamics, structure, and intensity change.

Numerical studies have confirmed the presence of the TCDC at both the genesis and mature stages of the TC (Melhauser and Zhang 2014; Navarro and Hakim 2016;

✉ Gabriel J. Williams Jr.
williamsgj@cofc.edu

1 Department of Physics and Astronomy, College of Charleston, Charleston, SC, USA

Ruppert and O'Neill 2019). Using the operational HWRF model, Bu et al. (2014) examined how the interaction of hydrometeors with atmospheric radiation can influence TC structure and intensity. This study demonstrated that cloud radiative forcing enabled hydrometeors to modulate radiative tendencies in the outflow layers, and the presence of cloud radiative forcing produced storms with (1) more convection and diabatic heating outside the eyewall, (2) a wider eye, (3) a broader wind field, and (4) a stronger secondary circulation. Using the Advanced Research version of the WRF Model (WRF-ARW), Tang and Zhang (2016) examined the impacts of the diurnal radiation on the evolution of Hurricane Edouard (2014). They found that evening destabilization was a key factor in stimulating convection outside the TC inner core, which led to the development of outer rainbands and increased the size of the storm. O'Neill et al. (2017) examined diurnal responses to simulated TCs and found that internal inertial gravity waves are favored to form outside the TC inner core and that the anticyclonic outflow region of the storm is most receptive to these radially propagating features.

The above studies primarily focused on the impact of the TCDC on the middle- and upper-level structure of a TC. However, there have been comparatively fewer studies that have focused on the impact of the TCDC on the tropical cyclone boundary layer (TCBL). The most recent observational study on the boundary layer structural changes in response to the diurnal cycle in TC conditions was conducted by Zhang et al. (2020). This study analyzed data from 2242 GPS dropsondes in mature TCs to investigate the diurnal variation of the mean structure of the TCBL. It is found that the TCBL inflow is stronger and deeper at night than in the afternoon. The boundary layer equivalent potential temperature θ_e is also larger in the evening than in the daytime, especially for radii greater than 150 km. The relative humidity is larger both in the inner core ($R < 100$ km) and outer-core regions in the evening than in the afternoon. Furthermore, the surface layer is more unstable in the outer-core region in the evening than in the afternoon. These results are largely consistent with the results from the hurricane nature run from Nolan et al. (2013) and its subsequent analysis in Dunion et al. (2019). In particular, Dunion et al. (2019) discovered three important results: (1) diurnal oscillations in TCBL moisture appear as periodic minima that are concentrated at a radius from 100 to 300 km; (2) there are marked alternating periods of enhanced (evening to early morning hours) and suppressed (mid-morning to afternoon hours) surface winds and low-level inflow each day, particularly along the periphery and just outside the TC's inner core; and (3) there is a maxima in peak precipitation in the late evening to early morning in the inner core and in the early to late morning farther from the storm center.

The goal of this paper is to explain the physical processes that drive the diurnal variation in the TCBL. An important question to address is the relationship between convection and TCBL inflow during the TCDC. Enhanced convection associated with diurnal pulses could act to enhance upper-level outflow in the outer core of the TC during the day, which would cause enhanced TCBL inflow. On the other hand, enhanced TCBL inflow due to nocturnal radiative cooling could act to enhance surface enthalpy flux, which would cause enhanced convection. Thus, the question is: does the enhanced convection during the evening *drive* the enhanced TCBL inflow or does the enhanced TCBL inflow *drive* more convection? Furthermore, several hypotheses have been presented to explain the TCDC, such as convectively driven gravity waves (Pfister et al. 1993; Tripoli and Cotton 1989), radiatively reduced outflow resistance (Mecikalski and Tripoli 1998), cloud vs cloud-free differential heating (Gray and Jacobson 1977), and the seeder–feeder mechanism (Houze et al. 1981). This paper will examine which hypothesis best explains the observed diurnal variation in convection within the TCBL.

The paper will be organized as follows. Section 2 introduces the numerical model used in this study. Section 3 discusses the results of the control experiment, along with a description of the impact of the TCDC on the kinematic and thermal structure of the TCBL. Section 4 examines the relationship between convection and TCBL inflow during the TCBL, along with the physical processes which drive the diurnal variation of the TCBL. Section 5 examines the sensitivity of these results to cloud microphysics parameterization and radiation schemes. Implications and applications of this analysis will be given in Sect. 6.

2 Numerical model and parameters

The model used here is the axisymmetric, non-hydrostatic cloud model of Bryan and Fritsch (2002); Bryan and Rotunno (2009) (CM1, release 20.2). For the TC to achieve quasi-equilibrium in both intensity and in structure (Chavas and Emanuel 2014), solutions are obtained on a domain that is 3000 km wide and 25 km deep for a 120 day control simulation. A fixed horizontal resolution of 4 km is used to insure a spatially consistent radiative-convective equilibrium state. To accurately resolve the TCBL, a stretched vertical grid is employed, which starts with a grid spacing of 30 m and gradually increases to a grid spacing of 500 m at a height of 6.50 km. The grid spacing remains constant at 500 m above 6.50 km. The vertically stretched grid yields 20 model levels below 2 km. To minimize the reflectance of vertical propagating waves, a Rayleigh damping zone is introduced in the uppermost 5 km of the model and beyond the 2500 km radius of the model.

Sensible and latent heat fluxes are calculated using standard bulk aerodynamic formulas with surface exchange coefficients for momentum C_D based on Fairall et al. (2003) at low wind speeds and Donelan (2004) at high wind speed. The surface exchange for enthalpy C_E based on Drennan et al. (2007). Turbulence is parameterized using a Smagorinsky-type scheme in which the horizontal eddy viscosity depends on a prescribed horizontal length scale, chosen here to be 1500 m. The vertical length scale is a function of height that tends toward ku_*z near the surface, where k is von Karman's constant, u_* is the friction velocity, and z is height, and approaches 200 m as $z \to \infty$.

To simulate the effects of both longwave radiation and shortwave radiation, here we use the Rapid Radiative Transfer Model (RRTM-G) radiation scheme described in Mlawer et al. (1997) and Iacono et al. (2003). Interactive radiation allows convection to be generated by reducing the static stability as the atmosphere cools through emitting infrared radiation to space. Furthermore, radiation allows the simulated storm to achieve statistical equilibrium, maintain active convection, and produce robust variability. This scheme is designed for both accuracy and computational efficiency so that it may be used for long numerical integrations, as is the case here. The radiative effects of ice are treated as in Ebert and Curry (1992) with an effective radius for ice crystals of 50 μm. A fixed absorption coefficient of 0.0903614m^2 g^{-1} is assumed for liquid water, and a cloud fraction of one is assumed for all cloud layers. The carbon dioxide mixing ratio is set to 350 ppm (by volume), and since the stratosphere is constrained by the damping layer described above, the ozone mixing ratio is set to zero.

To simulate cloud microphysical processes, we use the Thompson et al. (2008) microphysics scheme. In addition to solving for the time tendencies of water vapor, cloud droplets, cloud ice, rain, snow, and graupel mixing ratios, this bulk parameterization scheme also allows the particle size distributions for rain, snow, and graupel to evolve in time. We set the assumed cloud droplet concentration to a typical maritime value of 100 cm^{-3}. One advantage of using this more complicated and expensive scheme is that it prevents the accumulation of liquid water in the upper troposphere during long simulations. This accumulation is an artifact of a zero fall-speed assumption in many warm-rain schemes for small mixing ratio, which also affects the radiative cooling rates in the upper troposphere.

This simulation excludes all external influences, such as varying sea surface temperature and wind shear, which allows for an identification of storm structure and intensity with the diurnal cycle of radiation. The sea surface temperature is fixed at 301 K, and the Coriolis parameter is constant at a value corresponding to 20° latitude. The solution is obtained for a fixed calendar day of 10 September 2020. A broad, weak vortex is introduced to the initial state, following Rotunno and Emanuel (1987), and the initial temperature and moisture profiles are taken from the Atlantic hurricane season observations described in Dunion and Marron (2008). We will now examine the overall structure of our simulated TC with special emphasis to the kinematic and thermal structure of the TCBL.

Figure 1 shows the time series of the maximum storm intensity, the maximum storm inflow, the radius of maximum winds, and the maximum surface precipitation rate. The initial development of the TC occurs at approximately around 25 km, and the radius of maximum wind (RMW) increases with time until day 30, as shown in Fig. 1c. This increase in the RMW coincides with an increase in storm size (not shown), a decrease in maximum radial inflow (as shown in Fig. 1b), a decrease in surface precipitation rate [as shown in Fig. 1d], and a gradual decrease in storm intensity [as shown in Fig. 1a]. From day 60 to day 80, the TC undergoes gradual intensification (which also coincides with a decrease in RMW, an increase in storm inflow, and an increase in surface precipitation during this time interval). From day 80 through the end of the simulation, the storm intensity fluctuates around a time-mean storm intensity of 76.5m s^{-1} with a standard deviation of 4.76m s^{-1}. During this same interval, the RMW of the storm gradually decreases from 60 to 30 km. These results indicate that the simulated storm has reached a quasi-equilibrium in intensity and in structure during this time interval (Chavas and Emanuel 2014). For the sake of this paper, we will refer to the quasi-equilibrium state of the simulated TC as the time period from day 80 to day 120 in the model simulation.

Next, we will examine the mean thermal and kinematic structure of the simulated TC during its quasi-equilibrium state. The azimuthal velocity, radial velocity, vertical velocity, and temperature of the simulated TC in its quasi-equilibrium state is given in Fig. 2. An azimuthal wind maximum is observed at a height of 1.3 km and a radius of 46 km [as shown in Fig. 2b] with a magnitude that is consistent with the time-series from Fig. 1a. The winds decay rapidly with both radius and height, and the azimuthal velocity becomes negative at radii greater than 400 km. The tropospheric temperatures [as shown in Fig. 2d] decrease nearly linearly with height with a mean lapse rate of -6.06K km^{-1} from the surface up to 13 km, consistent with the model simulations of Navarro and Hakim (2016). The magnitude of radial inflow approaches -20.0m s^{-1} near the inner core of the TC and extends from the RMW to over 600 km, as shown in Fig. 2a. Radial outflow is observed at a height of 12 km with a maximum magnitude near 12 m s^{-1}. Within the outer region of the storm, radial inflow is observed near a height of 9 km and extends from 250 to 400 km radii. The vertical velocity maximum approaches 4.00 m s^{-1} within the midtroposphere (as shown in Fig. 2c), and this maximum is connected to a
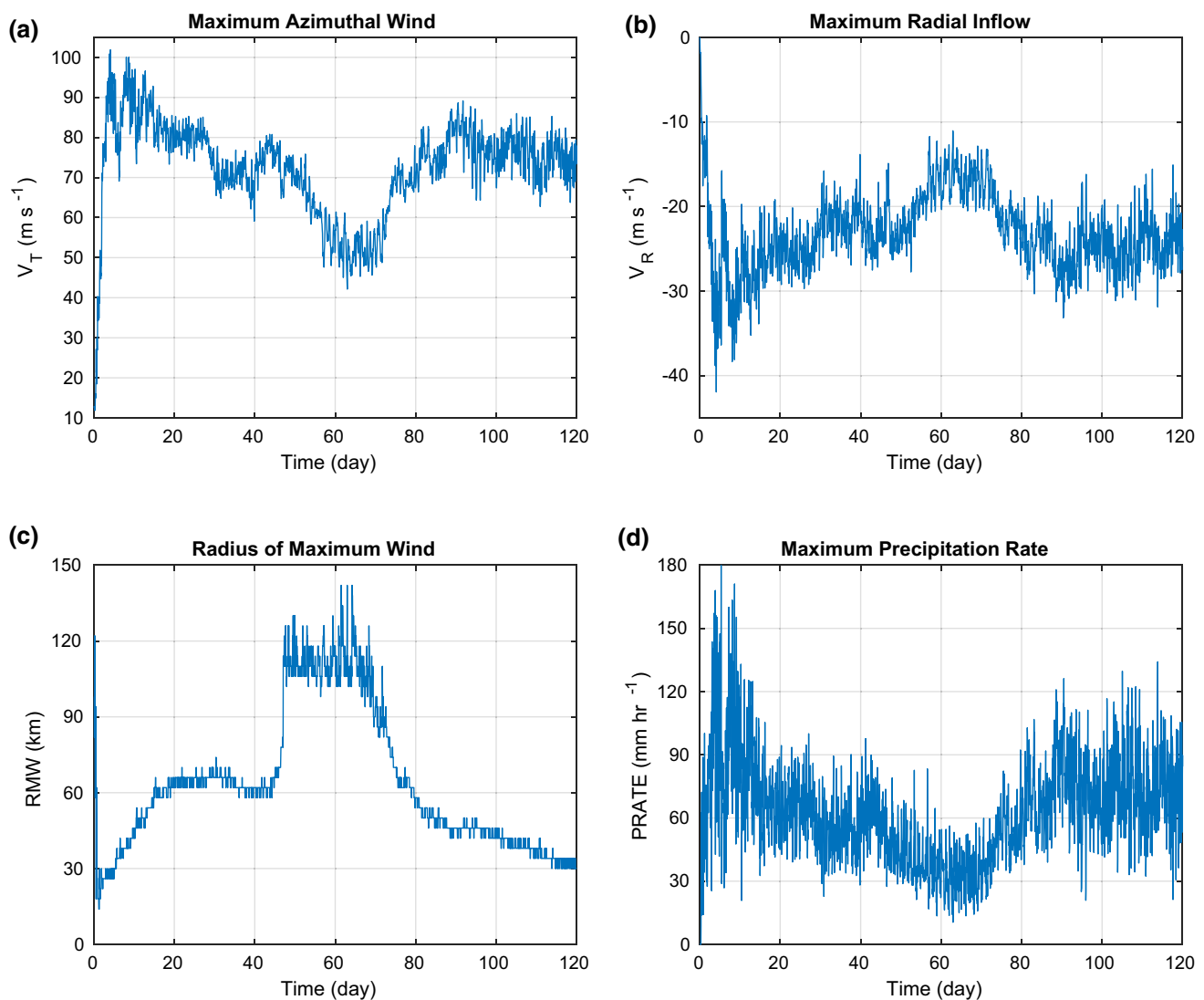
Fig. 1 Time series of **a** maximum azimuthal wind given in m s^{-1}, **b** maximum radial inflow given in m s^{-1}, **c** radius of maximum wind (RMW) given in km, and **d** maximum surface precipitation rate in mm hr^{-1}. For each time series, the sample frequency is 1.0 h

maximum in latent heating tendency within this region (not shown).

The kinematic and thermal fields of the TCBL for our simulated TC in its quasi-equilibrium state is given in Fig. 3. Compared to the observations of the TCBL in Zhang et al. (2011), the storm intensity is greater for the simulated TC, which is expected since the model simulation is axisymmetric and has reached its steady-state maximum intensity. Furthermore, the radial gradient of the radial and azimuthal velocity and the radial inflow are greater for the simulated TC. These are consistent with one another since a strong radial gradient in azimuthal velocity implies lower inertial stability outside of the RMW and a deeper TCBL (Kepert and Wang 2001; Kepert et al. 2016). Consistent with Zhang et al. (2011) and Williams (2016), the time-mean virtual potential temperature gradient,

as shown in Fig. 3d, can be divided into three distinct regions: a near-surface superadiabatic layer, a mixed layer, and a stable layer. The modeled region of superadiabatic lapse rate extends radially outward from the RMW to beyond 700 km, but it is confined to within 50 m of the surface. Consistent with the observations of mature TCs (Hawkins and Imbembo 1976; Montgomery et al. 2014), Fig. 3c indicates that the eyewall is characterized by conservation of θ_e with height, as would be expected by moist adiabatic ascent. Furthermore, a pronounced increase in θ_e occurs as the parcels decelerate after passing the RMW from approximately 345 K to above 360 K within the eye of the storm, consistent with previous observations (Bell and Montgomery 2008). A maximum in θ_e is located at the storm center, corresponding to a warm and moist anomaly, consistent with the observation that the air below the eye
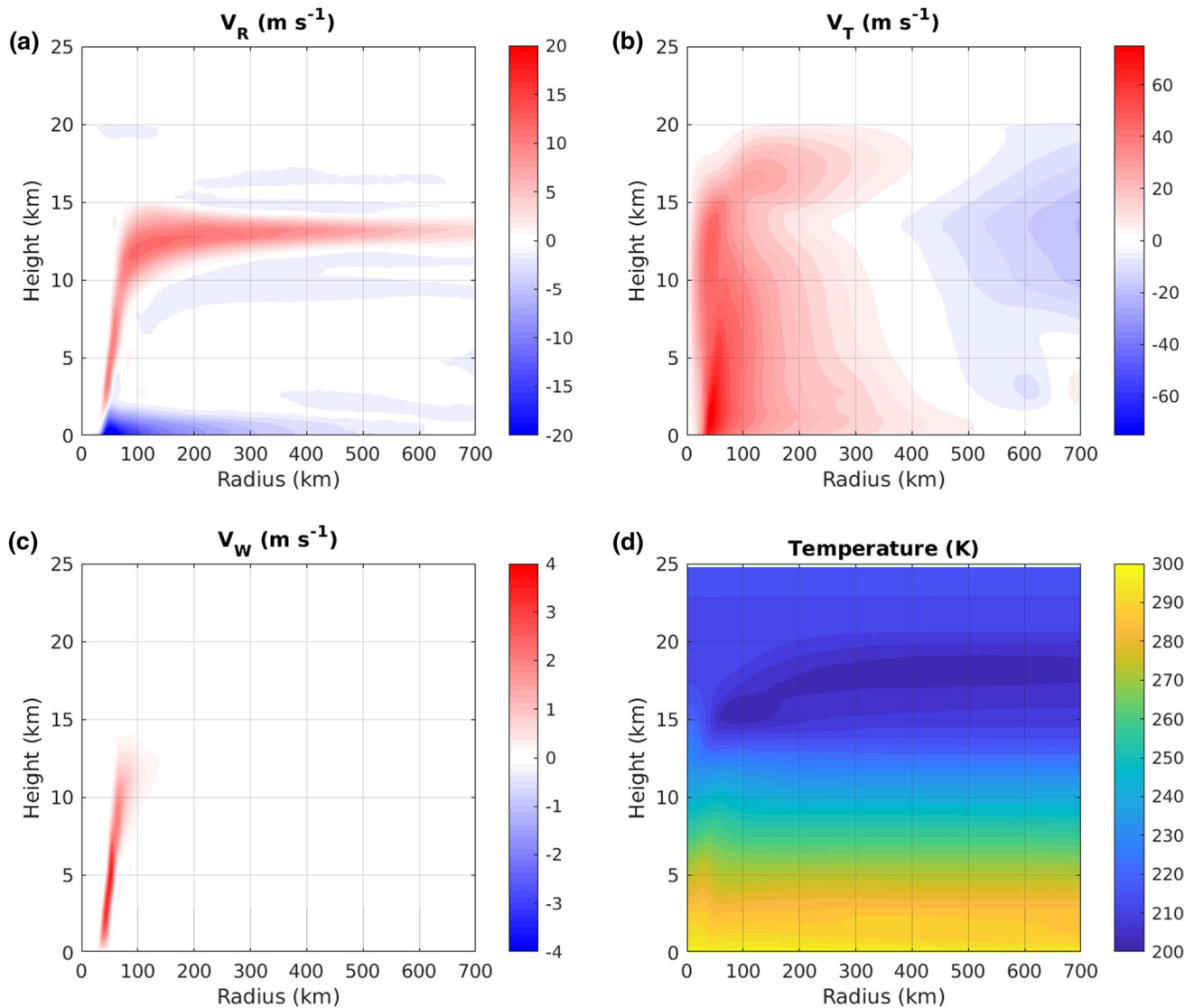
Fig. 2 The radius-height plot of the time-mean **a** radial velocity V_R given in m s^{-1}, **b** azimuthal velocity V_T given in m s^{-1}, **c** vertical velocity V_W given in m s^{-1}, and **d** absolute temperature given in K. For each plot, the radius and height are displayed in km, and the time-mean occurs over the quasi-equilibrium period (i.e., from day 80 to day 120) of the simulated TC

inversion has gained energy from upward heat and moisture fluxes from the ocean (Willoughby 1998).

3 Diurnal variation of the TCBL

In this section, we will describe the diurnal variation of the TCBL for our simulated TC. First, we will examine the model simulation from day 100 to day 120, which is a representative sample of the quasi-equilibrium period for our model simulation. Second, following the method of Dunion et al. (2014) and Zhang et al. (2020), the model results from day 100 to day 120 are grouped relative to the local time (LT) in four periods: night (0–6 LT), morning (6–12

LT), afternoon (12–18 LT), and evening (18–24 LT). Based on the observational analysis of the TCDC in Dunion et al. (2014) and Zhang et al. (2020), the differences in the composites between the night (0–6 LT) and the afternoon (12–18 LT) are expected to have statistically significant differences due to the TCDC.

Figure 4 shows the radius-height plots of azimuthal velocity and radial velocity within the TCBL for night (0–6 LST) and afternoon (12–18 LST) from day 100 to day 120. The overall structure of the azimuthal velocity plots (as shown in Fig. 4a, b) is similar between the night composite and afternoon composite with a maximum wind speed located at a height of approximately 1.5 km for both groups. However, the maximum azimuthal wind is slightly
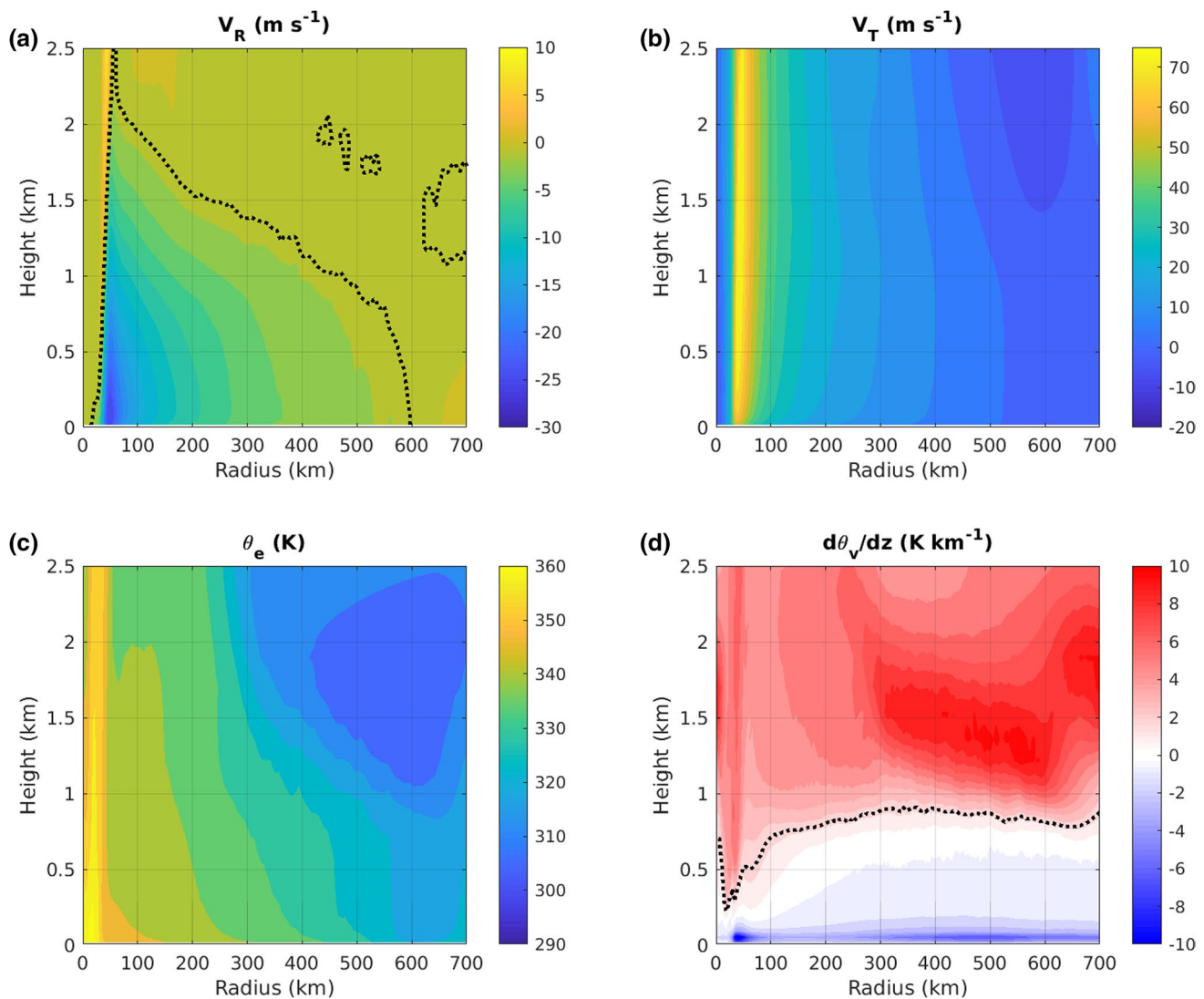
Fig. 3 The radius-height plot of the time-mean TCBL **a** radial velocity V_R given in ms^{-1}, **b** azimuthal velocity V_T given in m s^{-1}, **c** equivalent potential temperature θ_e given in K, and **d** virtual potential temperature gradient $d\theta_v/dz$ given in K km^{-1}. The black contour in (**a**) is the estimated kinematic boundary layer depth, defined as the height at which the radial velocity equals 10% of the peak inflow. The black contour in (**d**) is the estimated thermodynamic boundary layer depth, defined as the height at which $d\theta_v/dz = -2$ K km^{-1}. For each plot, the radius and height are displayed in km, and the time-mean occurs over the quasi-equilibrium period (i.e., from day 80 to day 120) of the simulated TC

stronger $\left(\approx 2ms^{-1}\right)$ in the night composite than in the afternoon composite. These findings are consistent with the observational study of Zhang et al. (2020) and are in general agreement with the modeling studies of (Nolan et al. 2013; Navarro and Hakim 2016 and Navarro et al. 2017). However, based on Fig. 4d–f, there is a clear difference in the radial wind between the night and afternoon periods. Within the outer core of the TC, there is a statistically significant difference in the radial inflow between the two composites with a deeper and stronger inflow layer in the evening in the outer region of the TC, and this difference

is statistically significant at 95% confidence based on the *t* test (not shown). Within the inner core of the TC, the peak inflow in the evening is slightly stronger in the evening composite than in the afternoon composite.

To examine the nature of the TCDC in the model simulation, Fig. 5 presents the kinematic fields averaged into four time windows (0–6, 6–12, 12–18, and 18–24 LST) and averaged into four radial regions (0–100, 100–250, 250–350, and 350–500 km) from day 100 to day 120, similar to that presented in Dunion et al. (2014) and Zhang et al. (2020). In the 0–100 km region (which represents the TC inner core), the structure of the radial inflow is
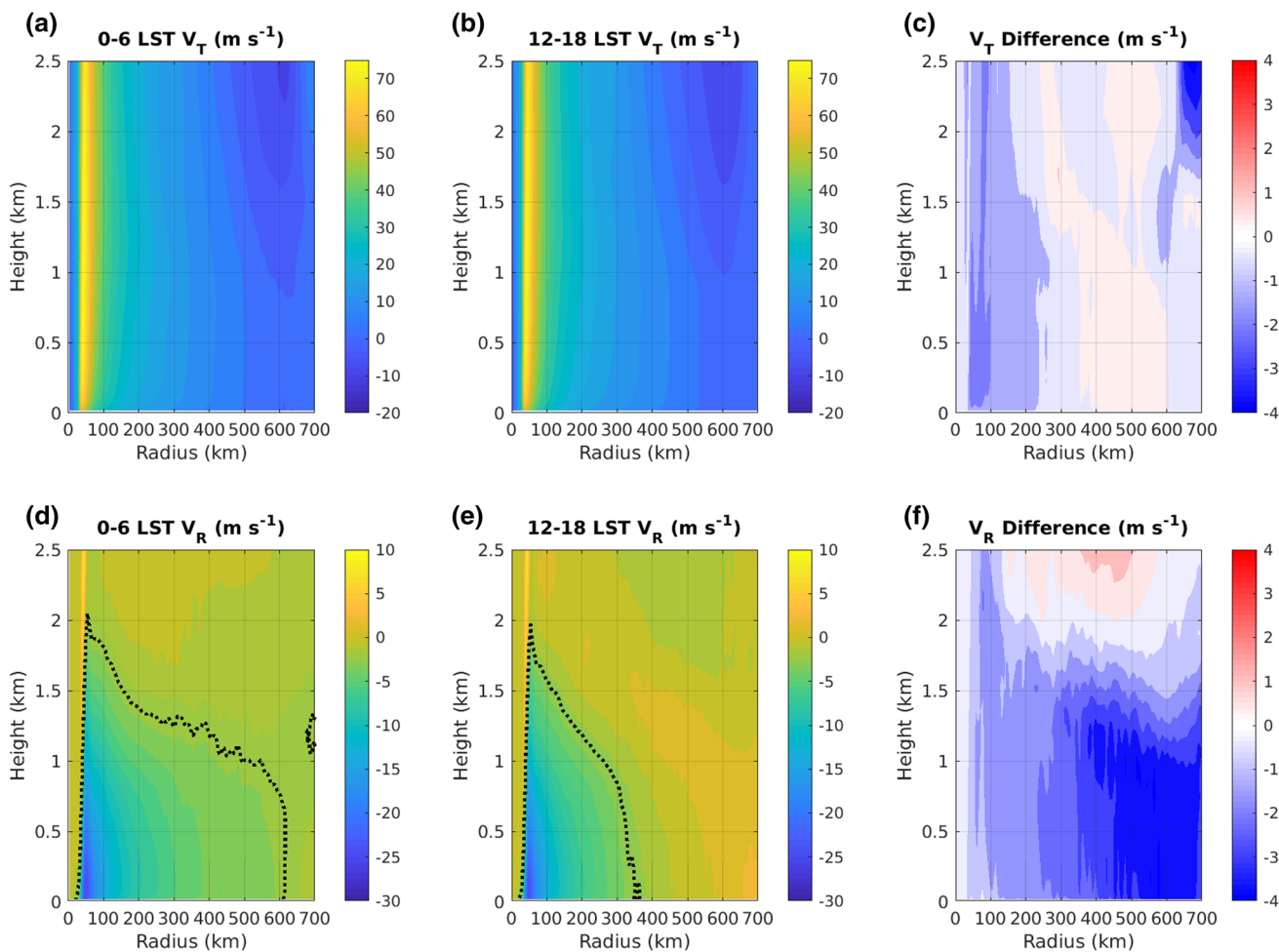
Fig. 4 **a–c** correspond to the radius-height plot for the time-mean azimuthal wind V_T for the 0–6 LST composite, for the 12–18 LST composite, and the V_T difference between these two composites, respectively. **d–f** Correspond to the radius-height plot for the time-mean radial wind V_R for the 0–6 LST composite, for the 12–18 LST composite, and the V_R difference between these two composites, respec- tively. The black contour in (**d**) and (**e**) is the estimated kinematic boundary layer depth, defined as the height at which the radial veloc- ity equals 10% of the peak inflow. For each plot, the radius and height are displayed in km, and the time-mean occurs from day 100 to day 120 of the simulated TC

nearly identical for the four time windows. However, as shown in Fig. 5e–h, the peak updraft and azimuthal wind are stronger in the morning hours (0–12 LST) than in the afternoon and evening hours (12–24 LST), especially outside of the inner core of the TC. In the region from 150–500 km, the peak inflow is the largest in the night composite (0–6 LST), while it is the smallest in the after- noon composite (12–18 LST) (as shown in Fig. 5b–d). The difference in peak radial inflow between these groups is as large as $3\,ms^{-1}$, which is consistent with the dropsonde composite analysis of Zhang et al. (2020) and with our previous analysis in Fig. 4. Furthermore, the inflow layer is deeper in the morning hours (i.e., 0–12 LST) than in the afternoon and evening hours (i.e., 12–24 LST). In the regions 250–350 and 350–500 km, we see that only inflow is observed below 1.5 km altitude for the 0–6 and 6–12

LST groups, whereas weak outflow is observed just below 1.5 km altitude for the 12–18 and 18–24 LST groups.

From the radial wind profiles in Fig. 5b–d, we observe that the inflow strengthens from the afternoon to the early evening, peaks after midnight, and then weakens through the morning hours. This behavior is reflected in the vertical velocity profiles in Fig. 5e–h. In the 100–250 km region, note that only upward vertical velocity is present up through 2.5 km for the 0–6 and 6–12 LST composites, whereas there is small subsidence in this region near 1.5 km for the 12–18 and 18–24 LST composites. This subsidence tends to weaken the convergence during these time intervals. In the 250–350 km and the 350–500 km regions, we observe a general pattern of upward vertical velocity near midnight that weakens into subsidence from 6 to 18 LST and intensi- fies through the late evening. This pattern of development
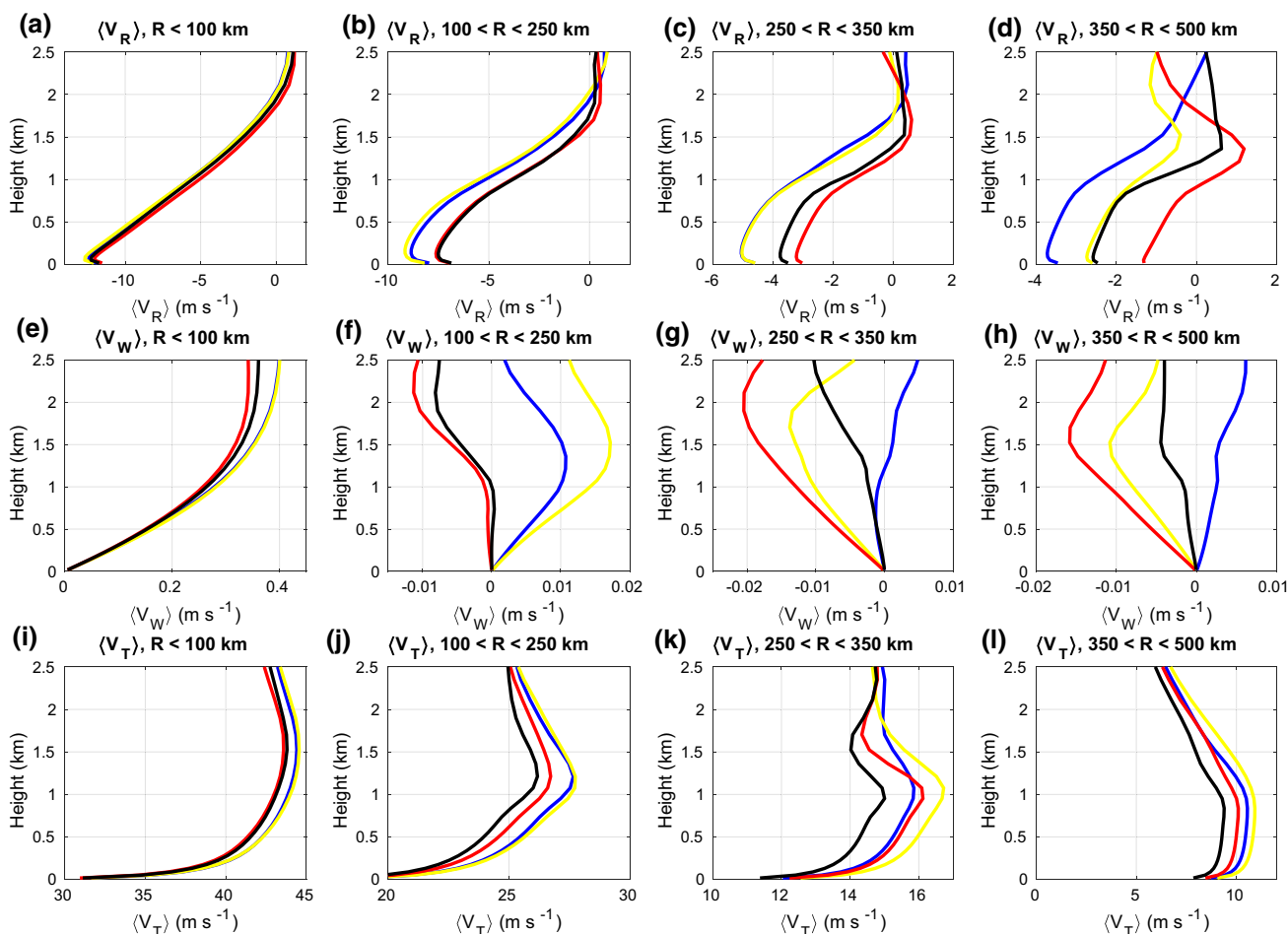
Fig. 5 **a–d** Correspond to the plots of vertical profiles of the time-mean radial velocity V_R, averaged for the regions $R < 100km$, $100 < R < 250km$, $250 < R < 350km$, and $350 < R < 500km$, respectively. **e–h** Correspond to the plots of vertical profiles of the time-mean vertical velocity V_W, averaged for the regions $R < 100km$, $100 < R < 250km$, $250 < R < 350km$, and $350 < R < 500km$, respectively. **i–l** Correspond to the plots of vertical profiles of the time-mean azimuthal velocity V_T, averaged for the regions $R < 100km$, $100 < R < 250km$, $250 < R < 350km$, and $350 < R < 500km$, respectively. The blue contour corresponds to the 0–6 LST composite, the yellow contour corresponds to the 6–12 LST composite, the red contour corresponds to the 12–18 LST composite, and the black contour corresponds to the 18–24 LST composite

suggests an expansion in the size of the secondary circulation in the TCBL during late evening hours to midnight and a contraction in the secondary circulation in the TCBL during the morning hours, consistent with Dunion et al. (2019) and Zhang et al. (2020). Consistent with a deeper and strong radial inflow, the azimuthal velocity is also generally stronger during the 0–6 and 6–12 LST groups, as shown in Fig. 5j–l. This behavior is most pronounced in the outer core of the TC where the azimuthal wind in the morning and evening composites are approximately $2 - 3$ m s^{-1} stronger than the afternoon composites.

To examine the impact of the TCDC on thermal structure of the TCBL, the radius-height plots of relative humidity, equivalent potential temperature, and virtual potential temperature gradient within the TCBL for night composite (0–6 LST) and afternoon composite (12–18 LST) from day 100 to

day 120 is presented in Fig. 6. We see in Fig. 6a–c that the relative humidity is significantly larger for the night composite than in the afternoon composite in the 350–500 km region. Comparing Fig. 6c to Fig. 5h, the decrease in relative humidity during the afternoon hours is related to the enhanced subsidence in this region. This tendency for the radial extent of low-level moisture to be enhanced in the night hours and suppressed during the afternoon hours was also found by Dunion et al. (2019). Figure 6d–f show that the equivalent potential temperature possesses almost identical structures within the inner core with the 345 K contour being nearly vertical in the eyewall. However, the largest difference in θ_e is seen near the top of the inflow layer near the 350–500 km region, where θ_e is statistically larger (according to a student t test) in the night composite than in the afternoon composite, consistent with the differences in
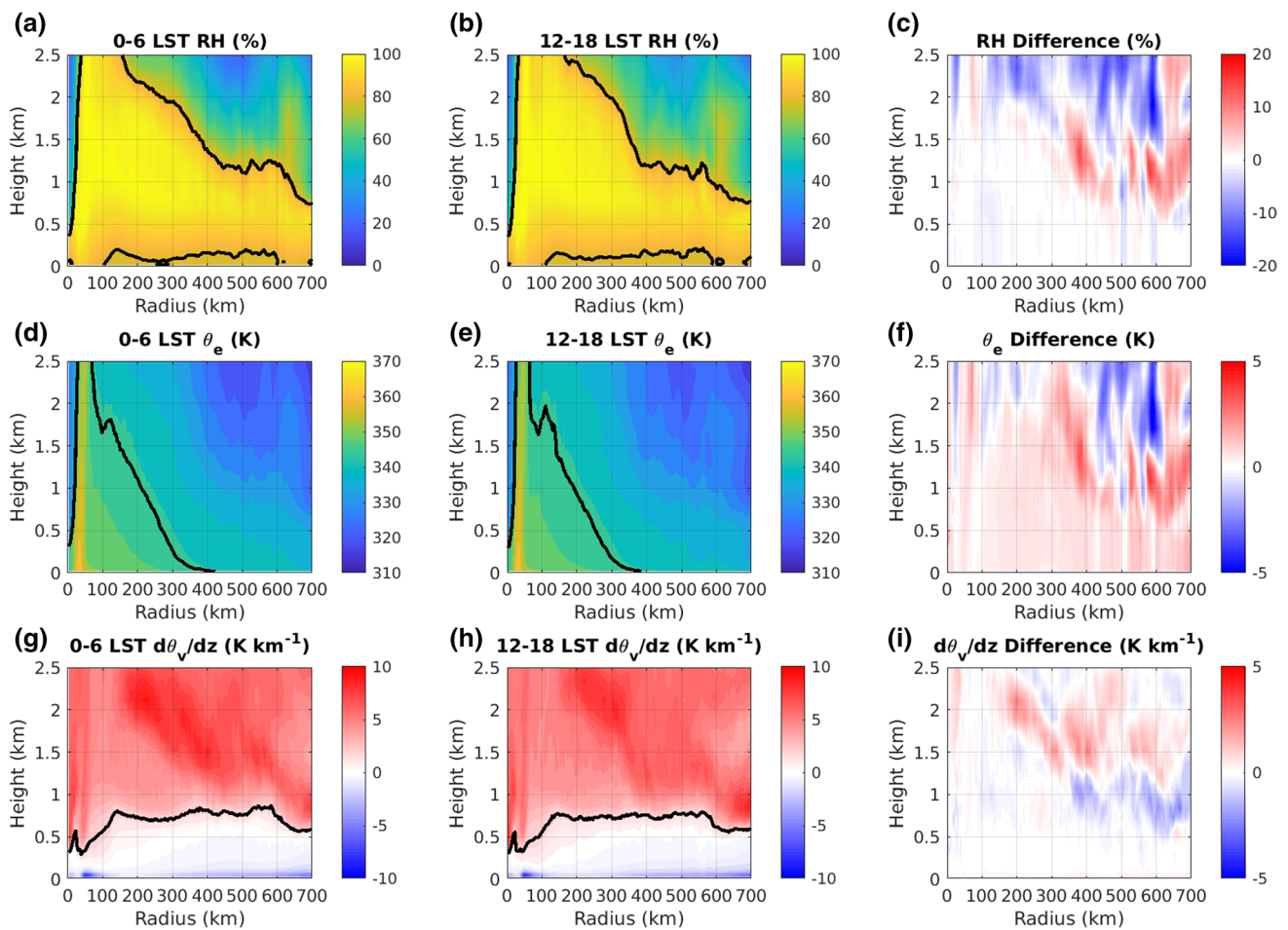
Fig. 6 **a–c** Correspond to the radius-height plot for the time-mean relative humidity (RH) for the 0–6 LST composite, for the 12–18 LST composite, and the RH difference between these two composites, respectively. The black contours in (**a–c**) corresponds to a relative humidity of 80%. **d–f** Correspond to the radius-height plot for the time-mean equivalent potential temperature θ_e for the 0–6 LST composite, for the 12–18 LST composite, and the θ_e difference between these two composites, respectively. The black contours in (**d–f**) Cor-respond to $\theta_e = 345K$. **g–i** The radius-height for the time-mean virtual potential temperature gradient $d\theta_v/dz$ for the 0–6 LST composite, for the 12–18 LST composite, and the $d\theta_v/dz$ difference between these two composites, respectively. The black contours in (**g–i**) are the estimated thermodynamic boundary layer depths, defined as the height at which $d\theta_v/dz = -2$ K km^{-1}. For each plot, the radius and height are displayed in km, and the time-mean occurs from day 100 to day 120 of the simulated TC

relative humidity as shown in Fig. 6c. Finally, the virtual potential temperature gradient $d\theta_v/dz$ is weaker in the night composite than in the afternoon composite near the top of the inflow layer in the outer regions of the TC, as shown in Fig. 6g–i. This indicates that that the thermodynamic mixed layer is less stable in evening, and this diurnal change in static stability is consistent with the upward vertical velocity found in this region in Fig. 5f–h. These results are qualitatively consistent with the observational analysis from Zhang et al. (2020), indicating that our model simulation is capturing the essence of the TCDC within the TCBL.

Since there is diurnal variability within the TCBL, it is expected that this these changes will also be reflected in the surface layer of the TC. To verify this, the radial profiles of the near-surface thermal fields for our four time windows

are given in Fig. 7. We see a clear diurnal variation in surface enthalpy flux (HFX) near a radius of 100 km. As Fig. 7a indicates, surface enthalpy flux increases in magnitude during the morning hours (i.e., from 0 to 12 LST) which is coincident with higher relative humidity (as shown in Fig. 7d) and lower LCL (as shown in Fig. 7h). During the afternoon hours, the surface enthalpy flux decreases in magnitude, leading to lower relative humidity and higher LCL. As shown in Fig. 7a, the surface enthalpy flux becomes negative during from 18 to 24 LST. The diurnal variation in relative humidity near the surface is also linked to the diurnal variation in surface precipitation rate in this region (as shown in Fig. 7e) as rain evaporation increases the water vapor mixing ratio in this region. Within the outer regions of the TC, we note that there is a clear diurnal variation in
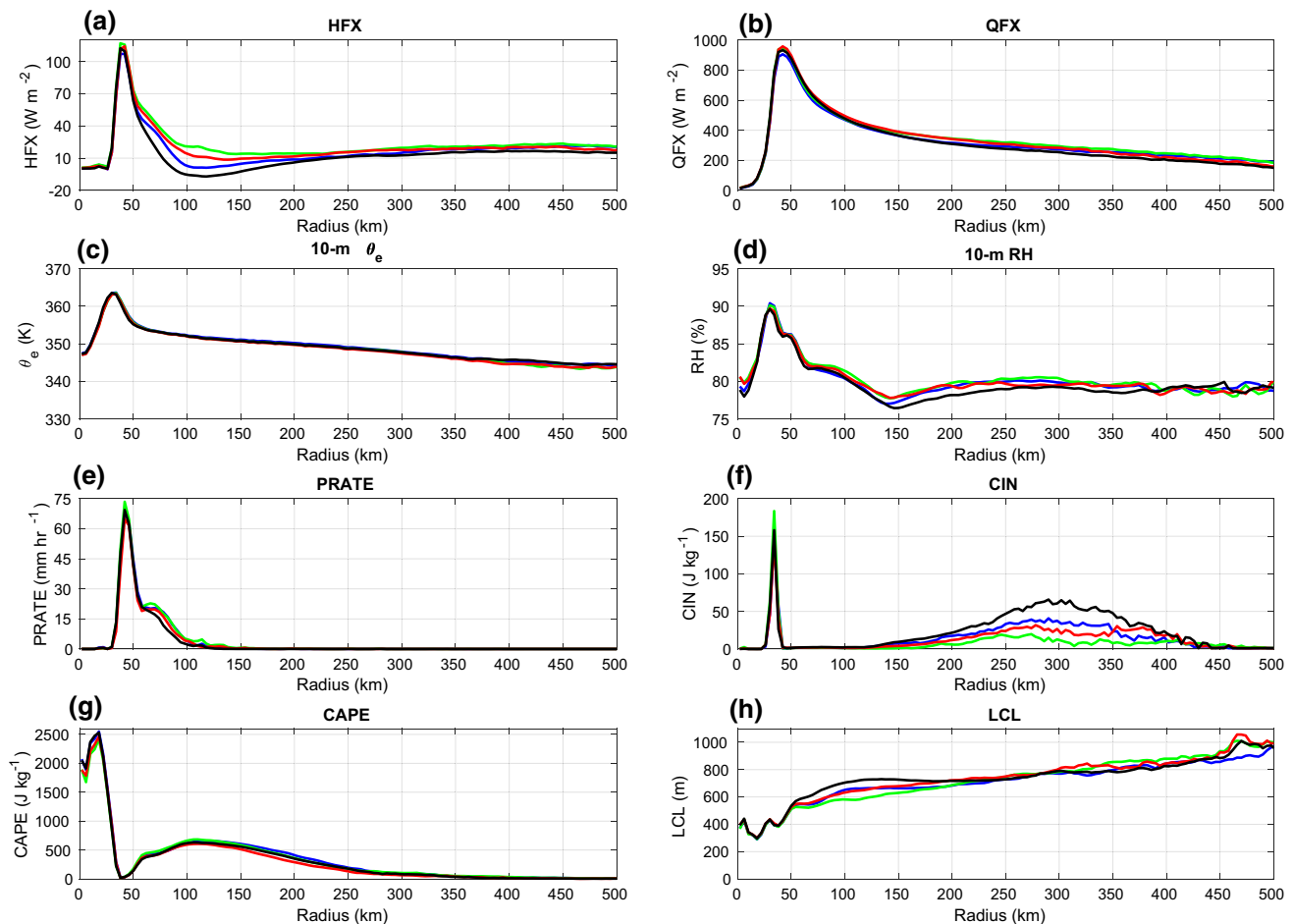
Fig. 7 Time-mean radial profiles of **a** surface enthalpy flux (HFX), **b** surface latent heat flux (QFX), **c** the 10 m equivalent potential temperature θ_e, **d** the 10 m relative humidity (RH), **e** the surface precipitation rate (PRATE), **f** the convective inhibition (CIN), **g** the convective available potential energy (CAPE), and **h** the lifting condensation level (LCL). The blue contour corresponds to the 0–6 LST composite, the green contour corresponds to the 6–12 LST composite, the red contour corresponds to the 12–18 LST composite, and the black contour corresponds to the 18–24 LST composite. The time-mean occurs from day 100 to day 120 of the simulated TC

convective inhibition (CIN) (as shown in Fig. 7f) such that CIN decreases during the morning hours (i.e., from 0 to 12 LST) and then increases during the evening hours (i.e., from 12 to 24 LST), which is consistent with the general pattern of TCBL static stability shown in Fig. 6i. Lastly, note that the maximum surface precipitation rate shown in Fig. 7e maximizes during the early morning hours, consistent with the pattern of tropical organized convection in Ruppert and Hohenegger (2018).

Finally, we will examine the diurnal variation in cloud-radiative forcing. Figure 8 shows the radius-height plots of temperature tendency due to longwave radiation (LWTEN), temperature tendency due to shortwave radiation (SWTEN), and cloud fraction (CLDFRA) within the TCBL for the night composite (0–6 LST) and the afternoon composite (12–18 LST) from day 100 to day 120. As shown in Fig. 8a–c, we note that the cloud fraction and the temperature tendency due to longwave radiation is significantly larger (in terms

of percentage) for the night composite (0–6 LST) than for the afternoon composite (12–18 LST). Conversely, the temperature tendency due to shortwave radiation (as shown in Fig. 8d–f) is significantly larger during the afternoon composite, which also corresponds to a minimum in cloud fraction as shown in Fig. 8h. The diurnal variation in these temperature tendencies is tied to the three-dimensional cloud distribution in the simulated TC as discussed in Dunion et al. (2019). Thus, in the morning hours (i.e., 0–6 LST), there is significant longwave radiative cooling at the cloud base with minimal shortwave radiative heating, which can act to destabilize the top of the inflow layer within the TCBL, which is consistent with the lapse rate mechanism from Randall et al. (1991). Conversely, in the afternoon to evening hours (i.e., 12–18 LST), the increase in shortwave radiative warming can act to stabilize the inflow layer within the TCBL. Comparing Fig. 8a to Fig. 7e, we see that the peak nocturnal longwave radiative cooling precedes the surface
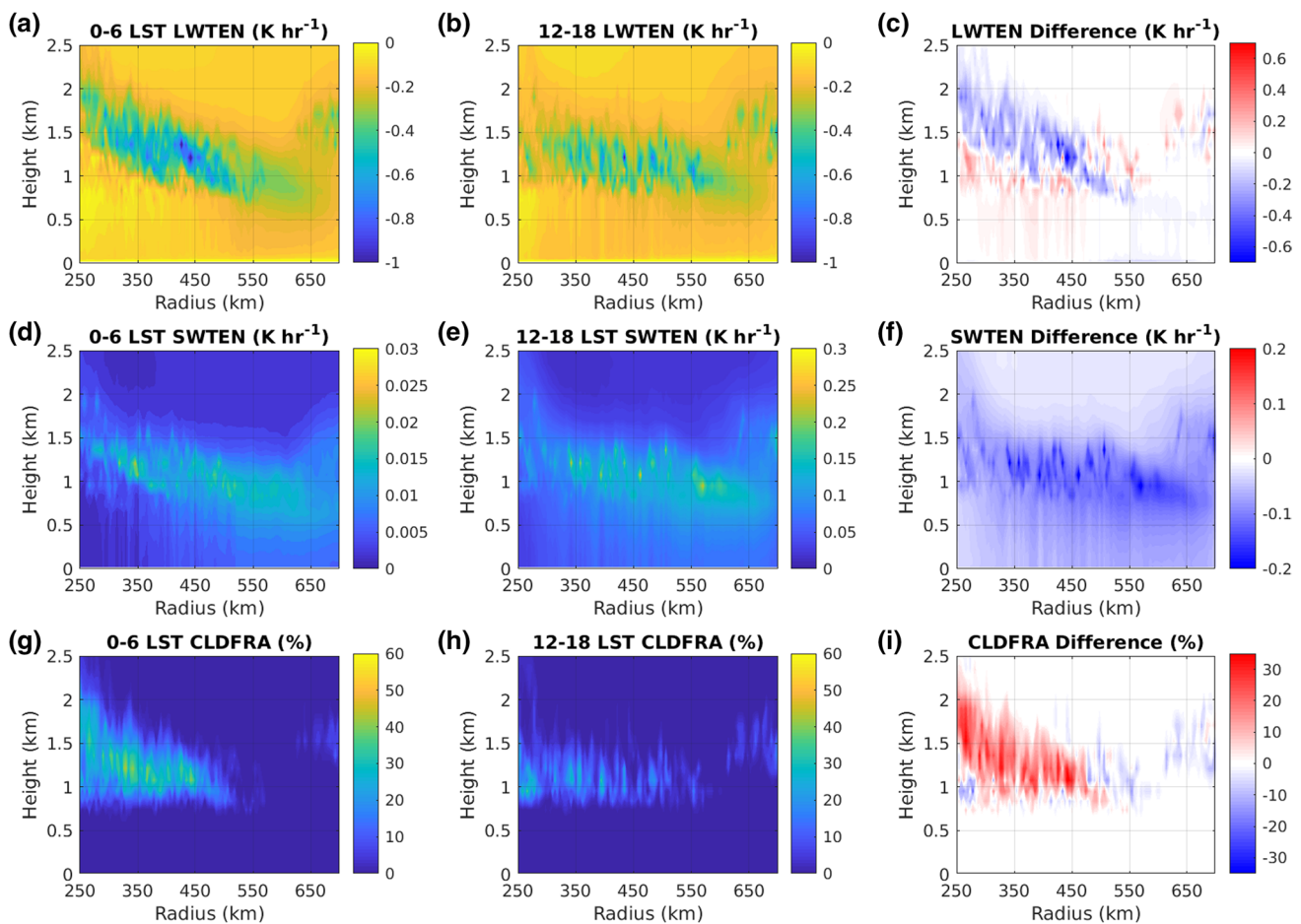
Fig. 8 a–c Correspond to the radius-height plot for the time-mean temperature tendency due to longwave radiation (LWTEN) for the 0–6 LST composite, for the 12–18 LST composite, and the difference between these two composites, respectively. **d–f** Correspond to the radius-height plot for the time-mean temperature tendency due to shortwave radiation (SWTEN) for the 0–6 LST composite, for the 12–18 LST composite, and the difference between these two composites, respectively. **g–i** Correspond to the radius-height for the time-mean cloud fraction for the 0–6 LST composite, for the 12–18 LST composite, and the difference between these two composites, respectively. For each plot, the radius and height are displayed in km, and the time-mean occurs from day 100 to day 120 of the simulated TC

precipitation maximum by approximately 6 h, consistent with the results of Ruppert and Hohenegger (2018).

In summary, the results from Figs. 4, 5, 6, 7, 8 provide a description of the diurnal cycle of the TCBL that is consistent with recent observational and modeling studies of mature TCs. The simulated TC develops a deeper, stronger, and less stable inflow layer during the evening hours and a shallower, weaker, and more stable inflow layer during the afternoon hours. These results are consistent with the signatures of a diurnal transverse circulation as shown in previous studies (Ciesielski et al. 2018; Navarro et al. 2017; Ruppert and O'Neill 2019). These studies illustrated an overnight intensification of bottom-heavy overturning, and a daytime suppression of low-level overturning but with the outflow both strengthened and lifted in response to shortwave radiative heating. In the following section, we will examine the physical processes which govern this transverse circulation

by examining the relationship between convection and the TCBL inflow during the TC diurnal cycle.

4 The relationship between convection and TCBL inflow

To determine whether enhanced evening convection causes enhanced TCBL inflow or vice versa, we will examine the statistical relationship between the time series associated with convection and TCBL inflow. If enhanced evening convection causes enhanced TCBL inflow, then it would be expected that there would be synchrony between the time series data associated with these variables. Moreover, it would be expected that there would be a persistent time-lag associated with these variables such that the release of convection would precede changes in TCBL inflow. To

quantify these relationships, the normalized cross-correlations and the time lags between latent heating tendency and the radial inflow from day 100 to day 120 of the simulated TC was computed. The cross-correlation for two discrete time-signals, x_n and y_n, is computed as

$$\hat{R}_{xy}(m) = \begin{cases} \sum_{n=0}^{N-m-1} x_{n+m} y_n^*, & m \geq 0 \\ \hat{R}_{yx}^*(-m), & m < 0 \end{cases} \quad (1)$$

where the asterisk denotes the complex conjugate and N corresponds to the length of the vector. The normalized cross-correlation is normalized so that the autocorrelations at zero lag equal 1. Thus, we have

$$\hat{R}_{xy,norm}(m) = \frac{\hat{R}_{xy}(m)}{\sqrt{\hat{R}_{xx}(0)\hat{R}_{yy}(0)}} \quad (2)$$

Table 1 presents the results of the cross-correlation analysis.

From Table 1, we see that inner-core latent heat tendency and the outer-core latent heat tendency are negatively correlated with radial inflow. This is to be expected since TC intensification is strongly tied to the release of convection. However, note that latent heating tendency and cloud fraction both possess a positive time-lag with the radial inflow in the outer core of the TC storm. Statistically, this indicates that changes in radial inflow tend to *precede* changes in latent heating tendency. This statistical result suggests that enhanced evening inflow within the TCBL *drives* enhanced evening convection. To further examine the physical processes that are responsible for enhanced radial inflow during the TC diurnal cycle, we will examine the potential temperature budget, moisture budget, and radial velocity budget.

4.1 Potential temperature budget

The potential temperature budget equation, following the notation of Bryan and Rotunno (2009), is given by

$$\frac{\partial \theta}{\partial t} = -u\frac{\partial \theta}{\partial r} - w\frac{\partial \theta}{\partial z} - \Theta_1 \theta \left(\frac{1}{r}\frac{\partial ru}{\partial r} + \frac{\partial w}{\partial z} \right)$$
$$+ \left[\Theta_2 \left(L_v \dot{q}_{cond} + L_s \dot{q}_{dep} + L_f \dot{q}_{frz} \right) + \Theta_3 \left(\dot{q}_{cond} + \dot{q}_{dep} \right) \right] \quad (3)$$
$$+ \Theta_2 \in + D_{\theta,H} + D_{\theta,V} + N_\theta + R$$

$$\Theta_1 = \left(\frac{R_m}{c_{vm}} - \frac{R_d c_{pm}}{c_p c_{vm}} \right), \Theta_2 = \frac{c_v}{c_{vm} c_p \Pi}, \Theta_3 = -\theta \frac{R_v}{c_{vm}} \left(1 - \frac{R_d c_{pm}}{c_p R_m} \right) \quad (4)$$

The budget terms associated with Eq. (3), from left to right, are radial advection; vertical advection; moisture

Table 1 The cross-correlation analysis associated with the inner-core latent heating tendency $\dot{\theta}_{COND,Inner}$, the outer-core latent heating tendency $\dot{\theta}_{COND,Outer}$, and the radial inflow for the simulated TC from day 100 to day 120

Variables	Normalized correlation	Lag (hours)
$\langle \dot{\theta}_{COND,Inner} \rangle, \langle V_R \rangle$	− 0.7814	2.0
$\langle \dot{\theta}_{COND,Outer} \rangle, \langle V_R \rangle$	− 0.7875	2.0

$\dot{\theta}_{COND,Inner}$ is computed by averaging the latent heating tendency radially in the region 30–50 km and by averaging vertically in the lowest 1 km. $\dot{\theta}_{COND,Outer}$ is computed by averaging the latent heating tendency radially in the region 350–500 km and by averaging vertically in the lowest 1 km. $\langle V_R \rangle$ is computed by averaging the radial wind radially in the region 350–500 km and by averaging vertically in the lowest 1 km. The normalized correlations and time lags are computed using the MATLAB algorithm

divergence; the potential temperature tendency from microphysical processes; dissipative heating; radial diffusion; vertical diffusion; Rayleigh damping; and temperature tendencies due to radiation, respectively.

Figure 9 shows the time-averaged vertical profiles of the potential temperature budget averaged into four radial regions (0–100, 100–250, 250–350, and 350–500 km) from day 100 to day 120 of the simulated TC. According to Fig. 9a, dissipative heating at the ocean surface is largely balanced by vertical diffusion (via upward surface enthalpy fluxes), radial advection, and cloud evaporative cooling within the inner core of the TC. Above the cloud base, warming due to condensation is primarily balanced by the strong cooling tendency due to vertical advection and vertical diffusion. Below cloud base in the inner core, the microphysical tendency term is negative (indicative of cooling due to cloud evaporation) and this cooling, combined with significant cooling from radial advection, is largely balanced by vertical diffusion. By comparing Fig. 9a to Fig. 6g–h, we note that the location of the stable layer in the TCBL occurs in the region in which the microphysical tendency term switches sign (i.e., around the cloud base of the TC). Outside of the inner core, warming due to condensation and cooling due to evaporation are primarily balanced by vertical diffusion to first order. As shown in Fig. 9c, d, longwave radiative cooling begins to play an important role in the potential temperature budget with peak radiational cooling occurring near the cloud base in the 250–350 and the 350–500 km regions, as expected from the temperature tendency due to longwave radiation in Fig. 8a, b.

To examine the impact of the TCDC on thermal budget of the TCBL, the vertical profiles of the dominant terms in the potential temperature budget averaged into three radial regions (100–250, 250–350, and 350–500 km) and averaged into four time windows (0–6, 6–12, 12–18, and 18–24 LST) from day 100 to day 120 of the simulated storm is given in Fig. 10. Based on the budget terms, there
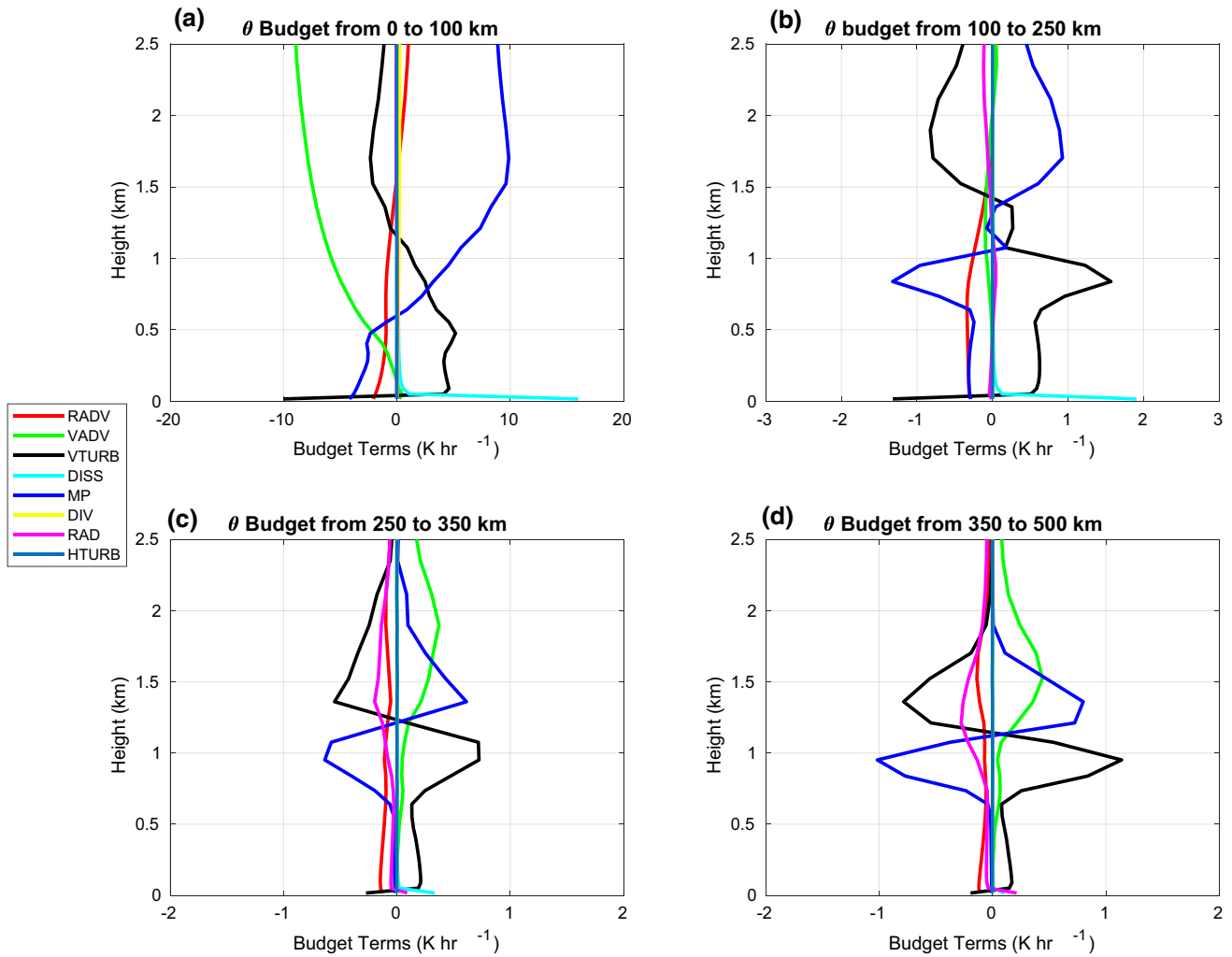
Fig. 9 Time-mean vertical profiles of potential temperature θ budget terms at **a** R < 100 km, **b** 100 < R < 250 km, **c** 250 < R < 350 km, and **d** 350 < R < 500 km measured in K hr^{-1}. *RADV* stands for radial advection, *VADV* stands for vertical advection, *VTURB* stands for vertical diffusion, *DISS* stands for dissipative heating, *MP* stands for microphysical processes, *DIV* stands for moisture divergence, *RAD* stands for radiation, and *HTURB* stands for horizontal diffusion. For each plot, the time-mean occurs from day 100 to day 120 of the simulated TC

is a clear diurnal cycle in the thermal forcing within the TCBL. As shown in Fig. 10a, b, longwave radiative cooling maximizes during the morning composite (0–6 LST), and it is primarily balanced by warming due to condensation from cloud formation, as shown in Fig. 10e, f. Immediately below the cloud base, there is a maximum in cooling due to cloud evaporation during the night composite (0–6 LST) (as shown in Fig. 10e, f) and this is primarily balanced by vertical diffusion, as shown in Fig. 10g, h. By comparing Fig. 10e, f to Fig. 6g, h we see that the region of maximum radiational cooling for the morning composite (0–6 LST) is co-located with reduced static stability near the top of the inflow layer in the outer region of the TC. This indicates that the vertical gradient in longwave radiative cooling (as shown in Fig. 10a, b) reduces static

stability near the cloud base. This suggests that cloud formation within the TCBL may act to further destabilize the environment through the differential heating mechanism of Gray and Jacobson 1977.

4.2 Moisture budget

The budget equation for the water vapor mixing ratio is given by

$$\frac{\partial q_v}{\partial t} = -u\frac{\partial q_v}{\partial r} - w\frac{\partial q_v}{\partial z} + \left(\dot{q}_{cond} + \dot{q}_{dep}\right) + D_{\theta,H} + D_{\theta,V} \quad (5)$$

The budget terms associated with Eq. (5), from left to right, are radial advection; vertical advection; the water
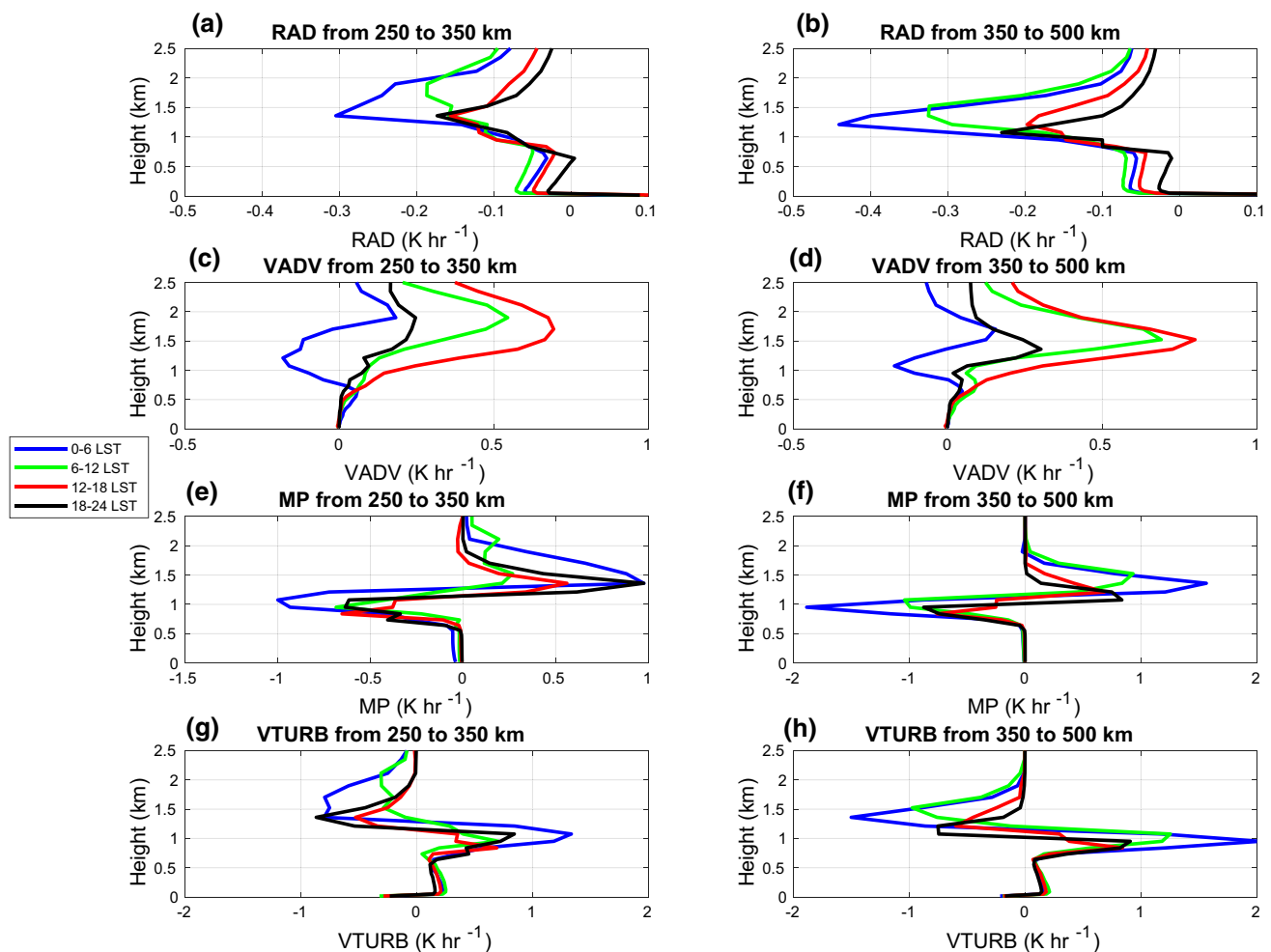
Fig. 10 Vertical profiles of potential temperature θ budget terms measured in K hr^{-1}. **a–b** Correspond to the radiation term (RAD) at $250 < R < 350$ km and $350 < R < 500$ km, respectively. **c–d** Correspond to the vertical advection term (VADV) at $250 < R < 350$ km and $350 < R < 500$ km, respectively. **e–f** correspond to the vertical diffusion term (VTURB) at $250 < R < 350$ km and $350 < R < 500$ km, respectively. **g–h** Correspond to the cloud micro- physics term (MP) at $250 < R < 350$ km and $350 < R < 500$ km, respectively. The blue contours correspond to the 0–6 LST composite, the green contours correspond to the 6–12 LST composite, the red contours correspond to the 12–18 LST composite, and the black contours correspond to the 18–24 LST composite. For each plot, the time-mean occurs from day 100 to day 120 of the simulated TC

vapor tendency from microphysical processes; radial diffusion; and vertical diffusion, respectively.

Figure 11 shows the time-averaged vertical profiles of the water vapor mixing ratio budget averaged into four radial regions (0–100, 100–250, 250–350, and 350–500 km) from day 100 to day 120 of the simulated storm. In general, the vertical profiles and horizontal distributions of the moisture budgets are like those of the potential temperature budget since their sources and sinks are related but are opposite in sign. As shown in Fig. 11a, we see that there is an approximate balance between radial advection, evaporation from precipitation (a source for water vapor), and vertical diffusion near the surface within the inner core of the simulated TC. Hence, radial advection transports drier air inward (leading to negative tendencies), which is offset by surface

rain evaporation and upward moisture flux from the ocean surface. Above the cloud base within the inner core, we note that cloud condensation (a sink for water vapor) is balanced by vertical advection and vertical diffusion of water vapor above the cloud base. Thus, despite the marked moisture loss by cloud condensation, the air column could still maintain a near-saturated condition because of the upward transport of moisture in the eyewall updrafts, consistent with the analysis of Williams (2019).

As shown in Fig. 11b (which represents the "moat" region of the TC), vertical advection plays a negligible role in the budget. Hence, radial advection within the inflow layer is primarily balanced by evaporation and vertical diffusion. In the outer region of the TC (i.e. $R > 150 km$), we see that radial advection of dry air near the surface is balanced by
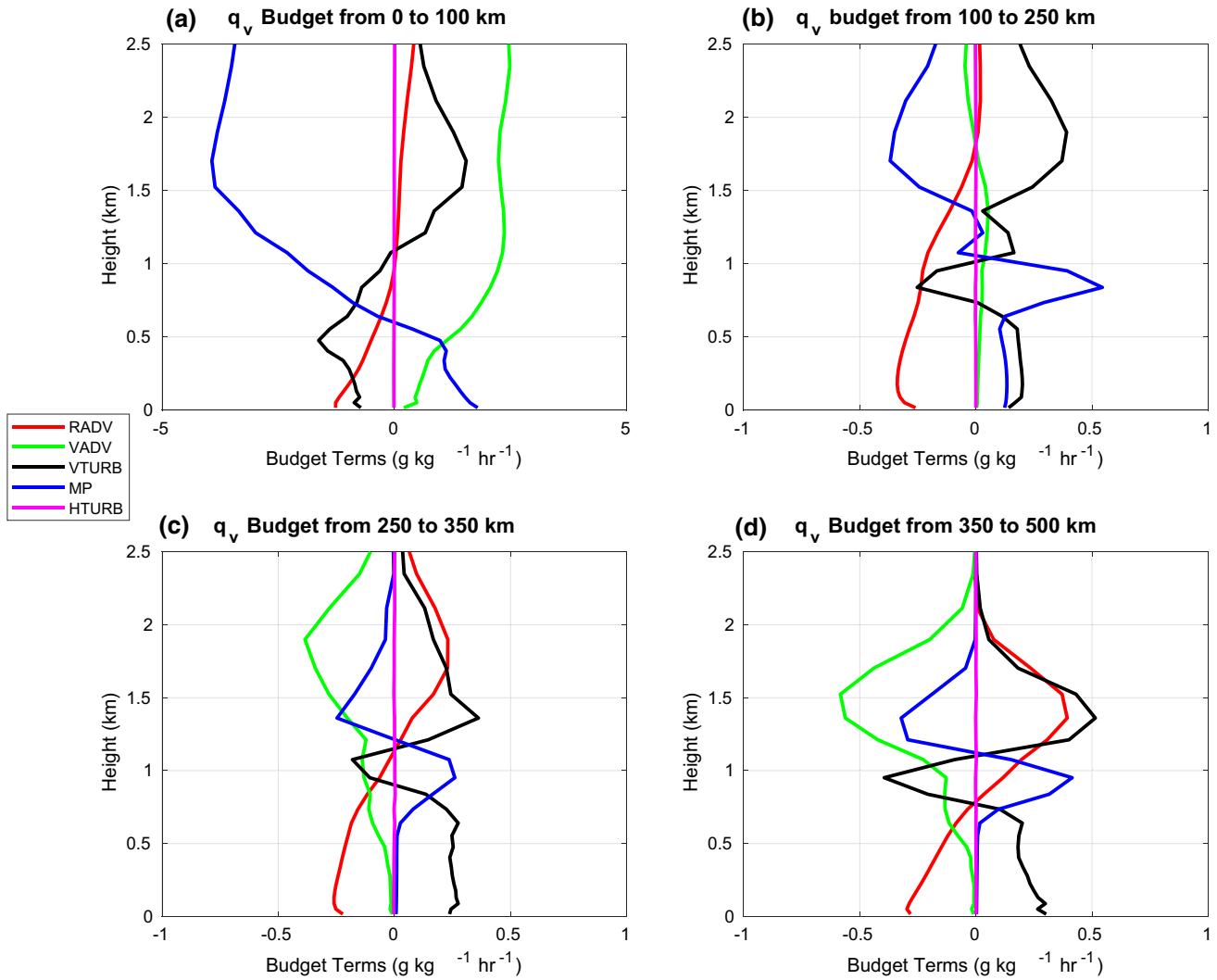
Fig. 11 Time-mean vertical profiles of water vapor mixing ratio q_v budget terms at **a** R < 100 km, **b** 100 < R < 250 km, **c** 250 < R < 350 km, and **d** 350 < R < 500 km measured at g kg^{-1} hr^{-1}. *RADV* stands for radial advection, *VADV* stands for ver-tical advection, *VTURB* stands for vertical diffusion, *MP* stands for microphysical processes, and *HTURB* stands for horizontal diffusion. For each plot, the time-mean occurs from day 100 to day 120 of the simulated TC

upward moisture flux from the ocean surface. Just below the cloud base, vertical advection and vertical diffusion of dry air are balanced by cloud evaporation. Above the cloud base, we see the radial advection and vertical diffusion are balanced by vertical advection and cloud condensation. Thus, the water vapor mixing ratio budget depends sensitively on the location of the cloud base as well as the cloud condensation rate in this region.

To examine the impact of the TCDC on moisture budget of the TCBL, the vertical profiles of the dominant terms in the water vapor mixing ratio budget averaged into three radial regions (100–250, 250–350, and 350–500 km) and averaged into four time windows (0–6, 6–12, 12–18, and 18–24 LST) from day 100 to day 120 of the simulated storm is given in Fig. 12. Just as in the potential temperature

budget, there is a clear diurnal cycle in the moisture forcing. As shown in Fig. 12e, f, cloud condensation and evaporation processes obtain their maximum amplitude in the night composite (0–6 LST), and these processes are primarily offset by vertical diffusion near the cloud base, as shown in Fig. 12g, h. Moreover, it should be noted that vertical moisture advection is positive near the cloud base for the night composite (0–6 LST) (as shown in Fig. 12c, d), and vertical advection becomes negative for the other three composites, consistent with the pattern of vertical θ advection in Fig. 10c, d. Radial advection also undergoes a diurnal pattern (as shown in Fig. 12a, b) in which its magnitude is larger during the evening and morning hours (0–12 LST), which is consistent with the deeper TCBL inflow during this region. By comparing Figs. 12a to Figs. 10a, we see that the region of
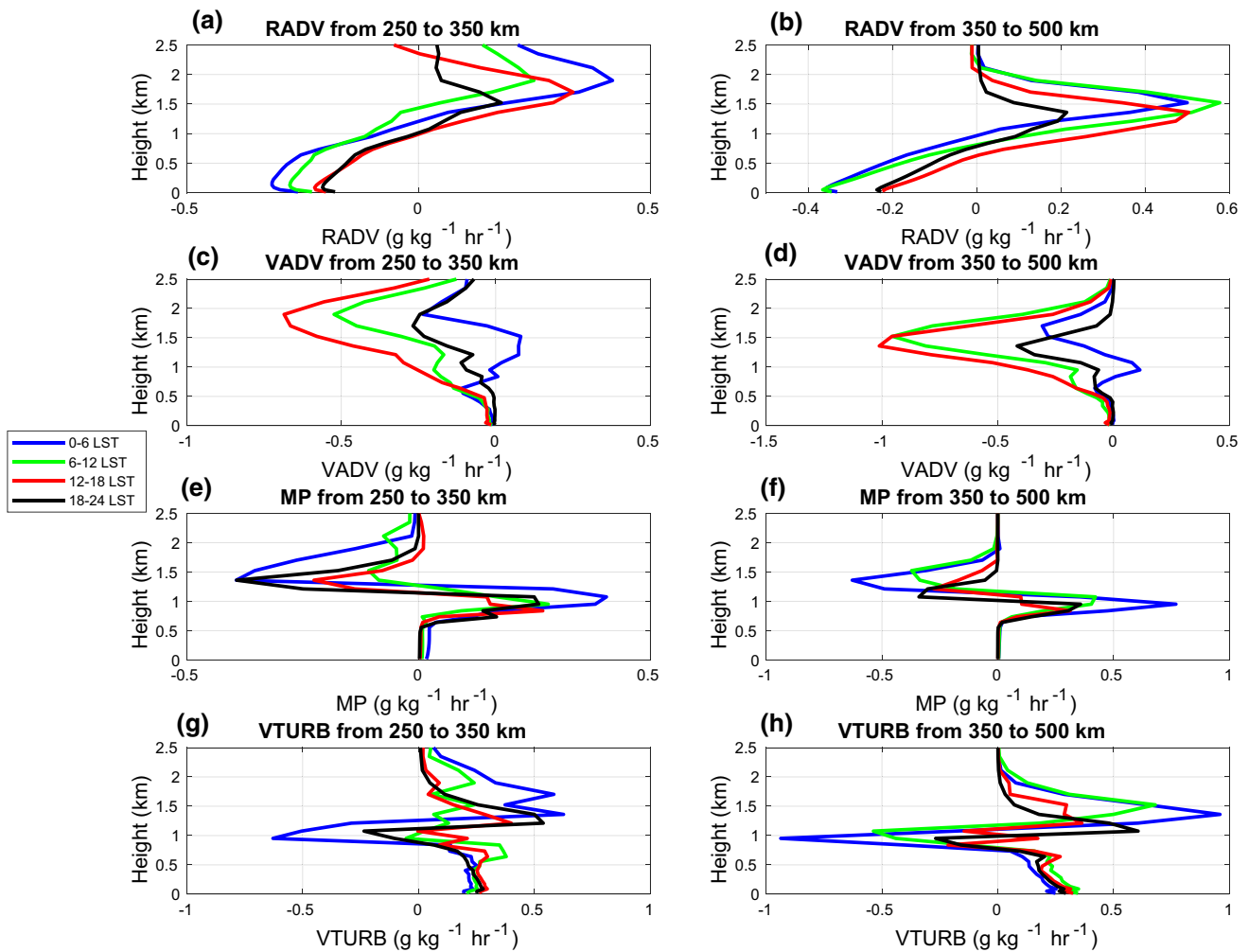
Fig. 12 Vertical profiles of water vapor mixing ratio q_v budget terms measured in $gkg^{-1}hr^{-1}$. **a–b** Correspond to the radial advection term (RADV) at 250 < R < 350 km and 350 < R < 500 km, respectively. **c–d** Correspond to the vertical advection term (VADV) at 250 < R < 350 km and 350 < R < 500 km, respectively. **e–f** Correspond to the vertical diffusion term (VTURB) at 250 < R < 350 km and 350 < R < 500 km, respectively. **g–h** Corre-spond to the cloud microphysics term (MP) at 250 < R < 350 km and 350 < R < 500 km, respectively. The blue contours correspond to the 0–6 LST composite, the green contours correspond to the 6–12 LST composite, the red contours correspond to the 12–18 LST composite, and the black contours correspond to the 18–24 LST composite. For each plot, the time-mean occurs from day 100 to day 120 of the simulated TC

maximum radiational cooling at the cloud top is co-located with the maximum radial moisture advection in this region. The combined effect of these processes is to increase relative humidity in the outer regions of the TC near the top of the inflow layer, as shown in Figs. 6a, b.

4.3 Radial velocity budget

According to Bryan and Rotunno (2009), the radial velocity budget equation for our numerical model is given by

$$\frac{\partial u}{\partial t} = -u\frac{\partial u}{\partial r} - w\frac{\partial u}{\partial z} + \left(f + \frac{v}{r}\right)v - c_p\theta_v\frac{\partial \pi'}{\partial r} + D_{u,H} + D_{u,V} + N_u \tag{6}$$

The budget terms associated with Eq. (6), from left to right, are radial advection; vertical advection; the Coriolis force; the centrifugal force, the radial pressure gradient force, radial diffusion; vertical diffusion; and Rayleigh damping, respectively.

Figure 13 shows the time-averaged vertical profiles of the radial velocity budget averaged into four radial regions (0–100, 100–250, 250–350, and 350–500 km) from day 100 to day 120 of the simulated storm. At the surface (where the flow is subgradient), there is a balance between the agradient force term (which is defined as the sum of the radial pressure gradient force, the Coriolis force, and centrifugal force) and vertical diffusion. Thus, the agradient force decelerates an inflowing parcel toward the TC inner core of the vortex
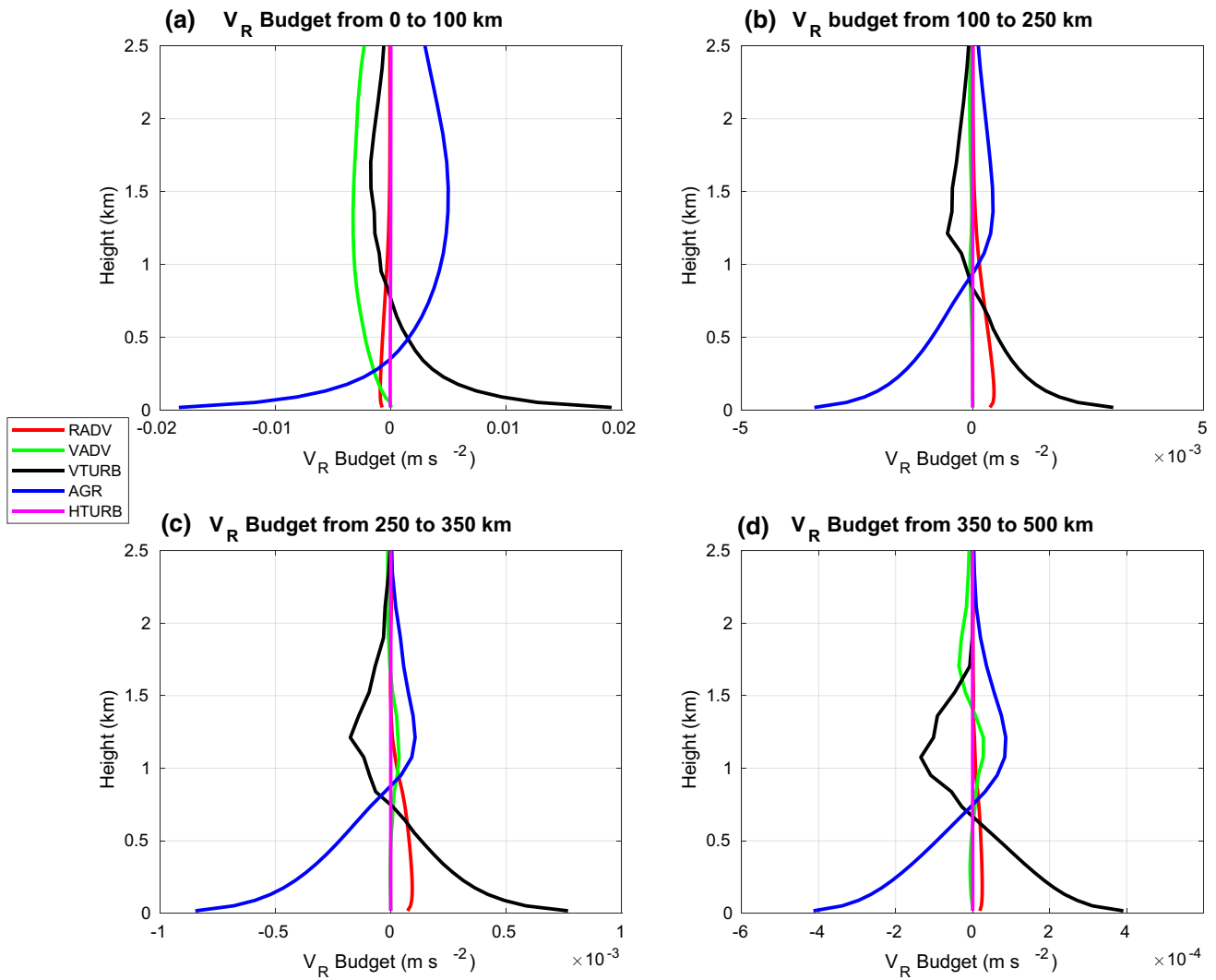
Fig. 13 Time-mean vertical profiles of radial velocity V_R budget terms at **a** R < 100 km, **b** 100 < R < 250 km, **c** 250 < R < 350 km, and **d** 350 < R < 500 km measured at m s^{-2}. *RADV* stands for radial advection, *VADV* stands for vertical advection, *VTURB* stands for ver- tical diffusion, *AGR* stands for agradient force (which is defined as the sum of the pressure gradient force, centrifugal force, and the Coriolis force), and *HTURB* stands for horizontal diffusion. For each plot, the time-mean occurs from day 100 to day 120 of the simulated TC

and vertical diffusion serves to balance these two processes near the surface. The agradient force switches signs at the top of the inflow layer, signifying a transition to an outward acceleration and this is largely balanced by vertical advection within the inner core and vertical diffusion outside the inner core.

To examine the impact of the TCDC on radial velocity budget of the TCBL, the vertical profiles of the dominant terms in the radial velocity budget averaged into three radial regions (100–250, 250–350, and 350–500 km) and averaged into four time windows (0–6, 6–12, 12–18, and 18–24 LST) from day 100 to day 120 of the simulated storm is given in Fig. 14. As shown in Fig. 14e–h, we note that the agradient force and vertical diffusion reach their largest magnitude during the morning hours (0–12 LST).

Due to the deeper radial inflow in the morning hours, the agradient force switches signs at a higher altitude in the morning hours as well. Furthermore, note that the magnitude of the agradient force is at a minimum during the late afternoon hours (18–24 LST). Although the radial and vertical advection play a smaller role in the budget, it should be noted by comparing Fig. 10a with Fig. 14c that the vertical advection of radial velocity is strongly nega- tively correlated with longwave radiative cooling, and that the longwave radiative cooling lags the vertical advection of radial velocity. This suggests that the radiative cooling in this region may cause the vertical advection of radial wind. This is consistent with the diurnal transverse cir- culation discussed previously. Since the radial advection of radial wind is positive in this region, this suggests that
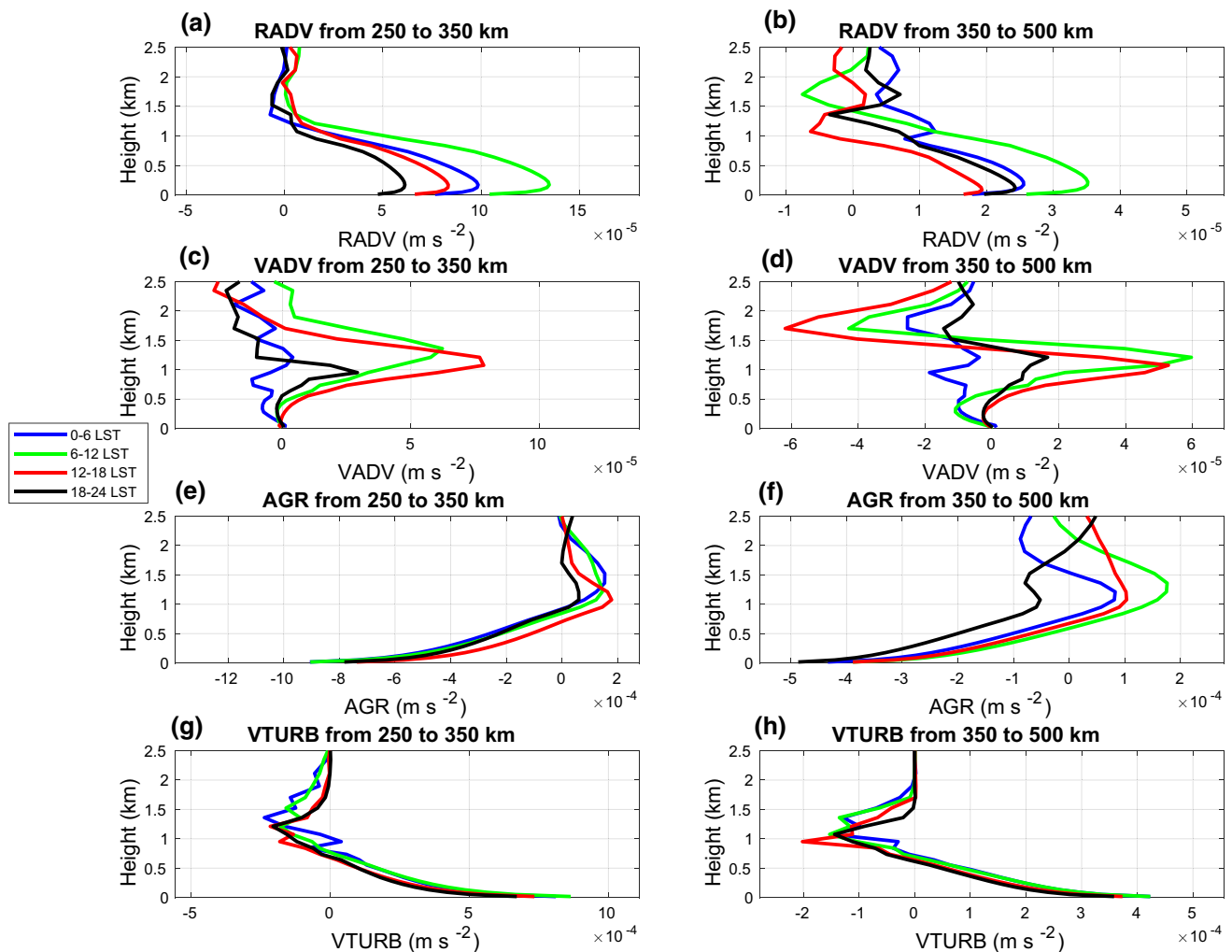
Fig. 14 Vertical profiles of radial velocity V_R budget terms measured in ms^{-2}. **a–b** Correspond to the radial advection term (RADV) at $250 < R < 350$ km and $350 < R < 500$ km, respectively. **c–d** Correspond to the vertical advection term (VADV) at $250 < R < 350$ km and $350 < R < 500$ km, respectively. **e–f** Correspond to the vertical diffusion term (VTURB) at $250 < R < 350$ km and $350 < R < 500$ km, respectively. **g–h** Correspond to the agradi-ent force term (AGR) at $250 < R < 350$ km and $350 < R < 500$ km, respectively. The blue contours correspond to the 0–6 LST composite, the green contours correspond to the 6–12 LST composite, the red contours correspond to the 12–18 LST composite, and the black contours correspond to the 18–24 LST composite. For each plot, the time-mean occurs from day 100 to day 120 of the simulated TC

radiational cooling locally generates radial outflow near the cloud base. From a balanced dynamics perspective, this outflow helps to enhance radial inflow below the cloud base (Ruppert and Hohenegger 2018).

5 Sensitivity to cloud microphysics and radiation scheme

To test the robustness of our previous results, we will show two additional model simulations with different combinations of cloud microphysics and radiation parameterizations. Each case is summarized in Table 2.

The control simulation, which is run with the Thompson microphysics parameterization and the RRTM-G radiation scheme, has been discussed in detail in Sect. 2. The Morrison parameterization refers to the three-ice class, double moment parameterization from Morrison et al. (2009). Unlike the Thompson parameterization, the Morrison parameterization predicts mixing ratios and number concentrations of all ice species, which improves the representation of the particle size distribution. For Case 1 and 2, graupel was used as the large ice category and the specified cloud droplet concentration was set to 100 cm^{-3}, which is consistent with typical maritime environment. The NASA-Goddard radiation scheme refers to the long-wave and shortwave radiation schemes that have been

Table 2 A summary of the microphysics parameterization and the radiation scheme used for each simulation

Case	Microphysics parameterization	Radiation scheme
Control	Thompson parameterization	RRTM-G radiation scheme
Case 1	Morrison parameterization	RRTM-G radiation scheme
Case 2	Morrison parameterization	NASA-Goddard radiation scheme

See the text for a description of each parameterization and radiation scheme

developed at NASA-Goddard for use in regional models (Chou and Suarez 1999, 2001).

5.1 Results from case 1

Figure 15 shows the radius-height plots of azimuthal velocity and radial velocity within the TCBL for the night composite (0–6 LST) and the afternoon composite (12–18 LST) from day 100 to day 120 for Case 1. By comparing Fig. 15 to Fig. 4, we see that there are many similarities in the kinematic structure of the TCBL between the control experiment and Case 1. Just as in the control experiment, the radial wind speed shows a clear difference between the evening and

afternoon periods. Within the outer core of the TC, there is a statistically significant difference in the radial inflow between the two composites with a deeper and stronger inflow layer in the evening in the outer core of the simulated TC. However, the inflow layer for Case 1 extended radially further than for the control experiment, and the azimuthal wind on the inner edge of the eyewall is stronger for Case 1.

Figure 16 shows the radius-height plots of relative humidity, equivalent potential temperature, and virtual potential temperature gradient within the TCBL for evening (0–6 LST) and afternoon (12–18 LST) from day 100 to day 120 for Case 1. First, we note that thermal structure of the TCBL for Case 1 is consistent with the control experiment. We see
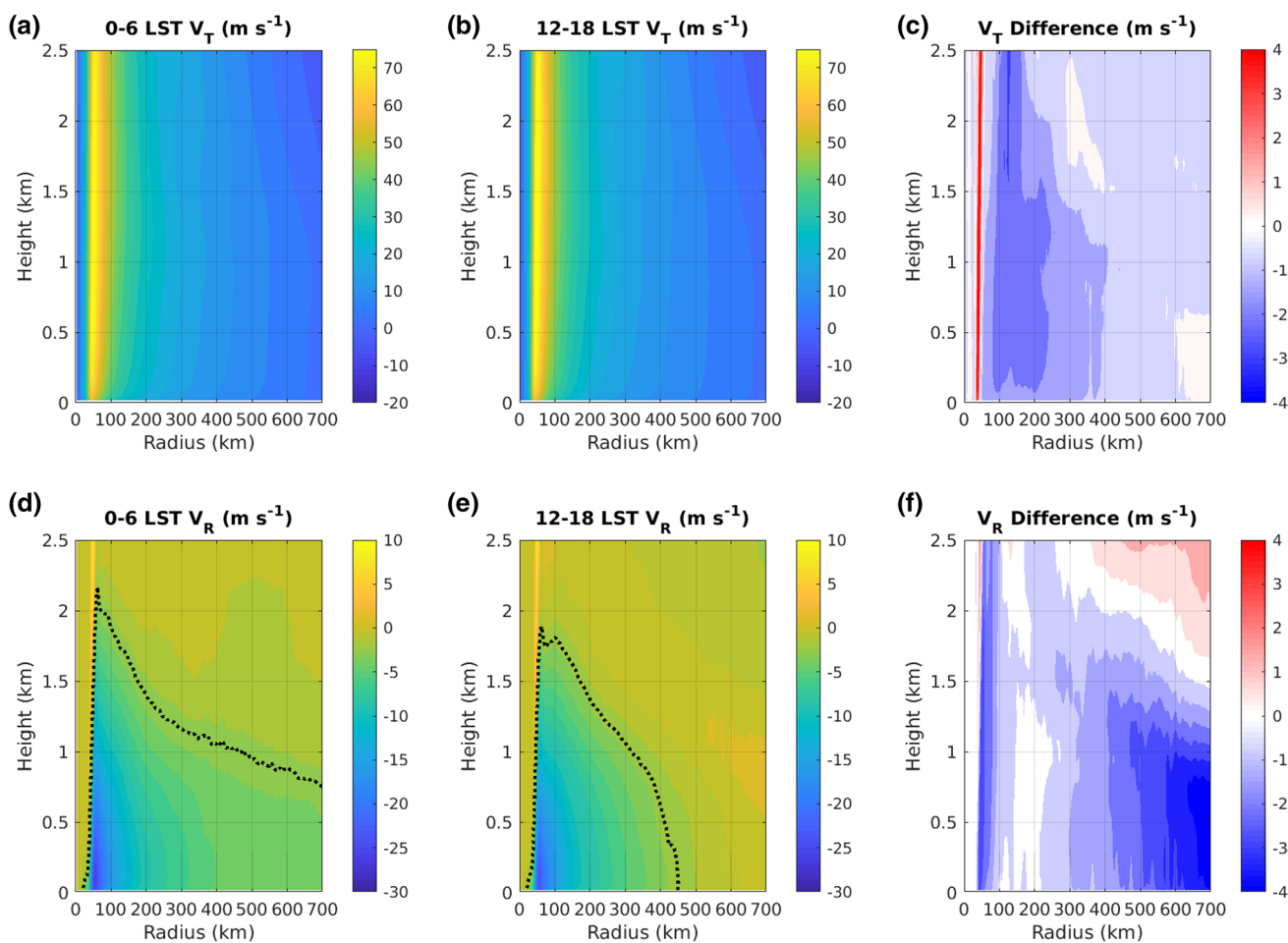

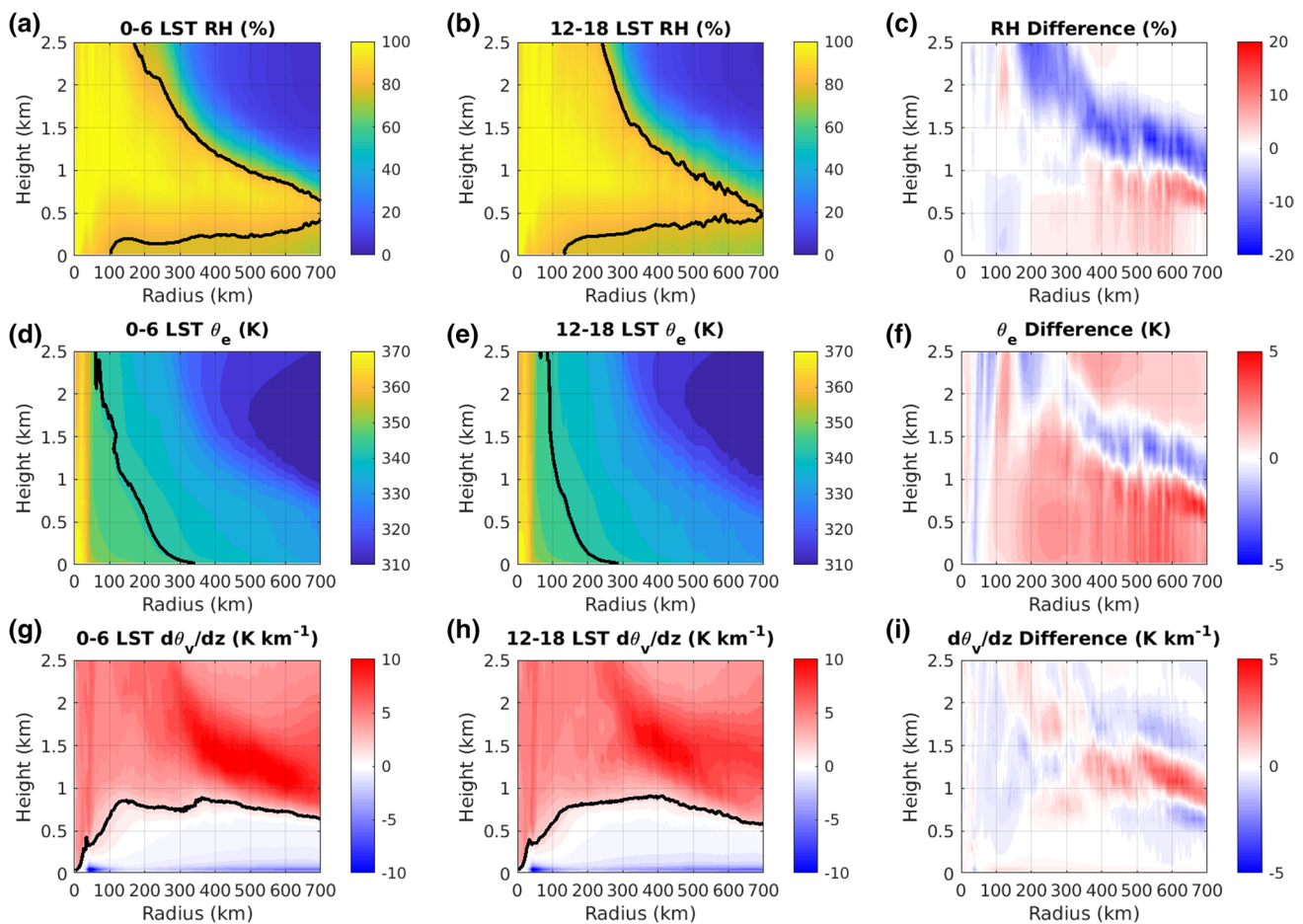**Fig. 15** Same as Fig. 4, except for the simulated storm for Case 1

Fig. 16 Same as Fig. 6, except for the simulated storm for Case 1

that the time-mean virtual potential temperature gradient for Case 1 possesses a near-surface superadiabatic layer, a mixed layer, and a stable layer. Moreover, we see that θ_e is approximately constant with height within the eyewall and strongly increases towards the eye of the storm with values above 360 K. Second, we see that the relative humidity (and thus θ_e) is larger at evening than in the afternoon in the outer core of the TC (i.e., in the 350–500 km region) near the top of the inflow layer, similar to the control experiment. Third, the virtual potential temperature gradient $d\theta_v/dz$ is weaker in the evening hours than in the afternoon composite near the top of the inflow layer in the outer regions of the TC, similar to the control experiment. By comparing Fig. 16 to Fig. 6, we note the diurnal difference in $d\theta_v/dz$ is consistently larger above the inflow layer for Case 1, and the diurnal difference in θ_e is consistently larger in the inflow layer for Case 1. A budget analysis of water vapor mixing ratio (not shown) indicates that the radial moisture advection is larger throughout the inflow layer for Case 1 than for the control experiment, which helps to explain the diurnal difference of θ_e in Case 1 compared to the control experiment.

Figure 17 shows the radius-height plots of temperature tendency due to longwave radiation (LWTEN), temperature tendency due to shortwave radiation (SWTEN), and cloud fraction (CLDFRA) within the TCBL for evening (0–6 LST) and afternoon (12–18 LST) from day 100 to day 120 for Case 1. Like the control experiment, we note that the cloud fraction and the temperature tendency due to longwave radiation is significantly larger at evening than in the afternoon, whereas the temperature tendency due to shortwave radiation is significantly larger during the afternoon hours. Thus, there is significant longwave cooling at the cloud top in the morning hours and shortwave radiative warming in the evening hours, just as in the control experiment. By comparing Fig. 17 to Fig. 8, the main differences between the control experiment and Case 1 are that the evening cloud fraction is larger for Case 1 and the evening cloud cover extends further radially for Case 1. A budget analysis of potential temperature (not shown) indicates that the increased cloud cover causes more radiative cooling near the cloud top, which affects the thermal stability of the TCBL for Case 1.
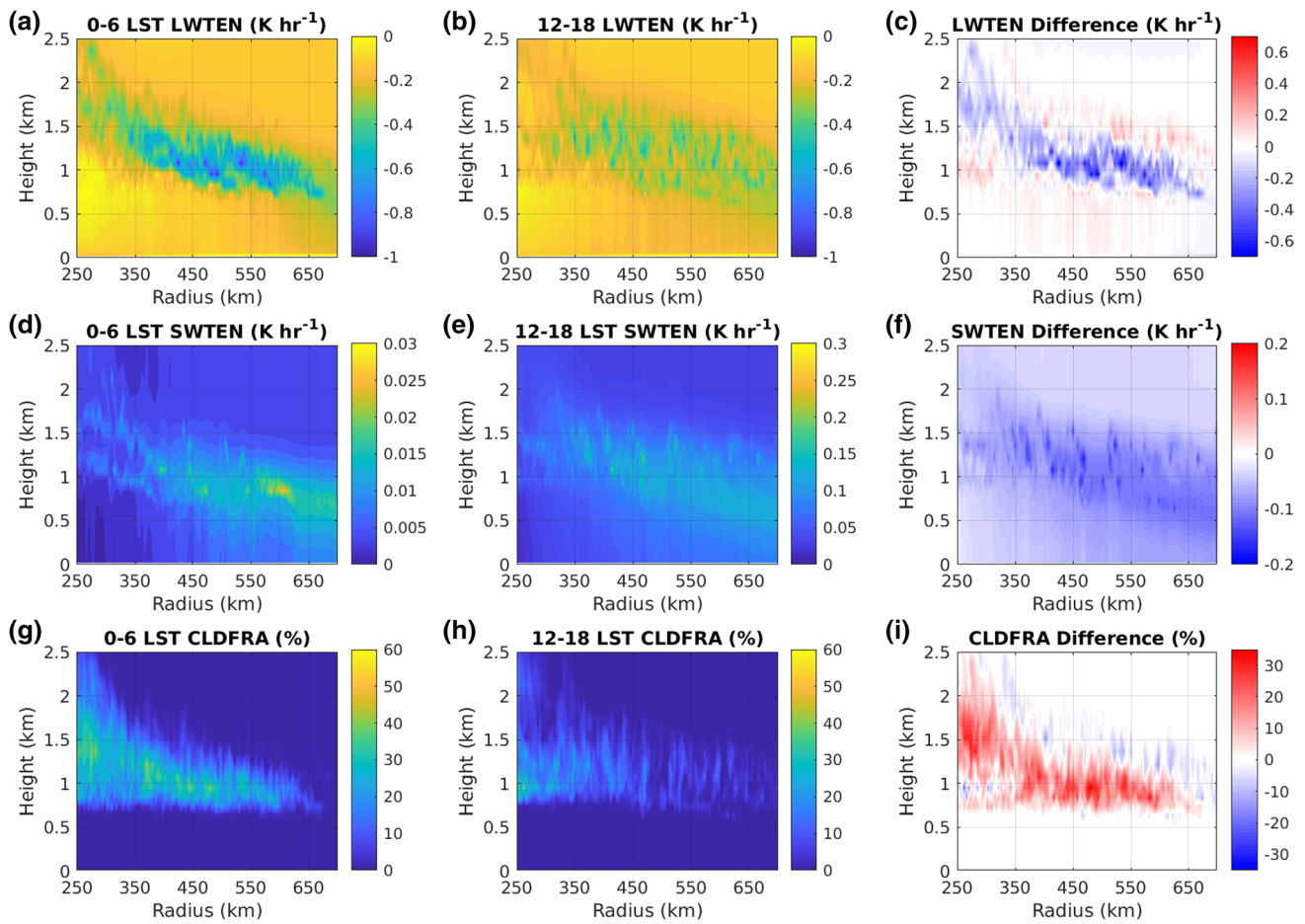
Fig. 17 Same as Fig. 8, except for the simulated storm for Case 1

Table 3 The cross-correlation analysis associated with the inner-core latent heating tendency $\dot{\theta}_{COND,Inner}$, the outer-core latent heating tendency $\dot{\theta}_{COND,Outer}$, and the radial inflow for the simulated TC in Case 1 from day 100 to day 120

Variables	Normalized correlation	Lag (hours)
$\langle \dot{\theta}_{COND,Inner} \rangle, \langle V_R \rangle$	− 0.6179	3.0
$\langle \dot{\theta}_{COND,Outer} \rangle, \langle V_R \rangle$	− 0.6729	2.0

The variables are defined and calculated in the same manner as discussed in Table 1

Table 3 presents the results of the cross-correlation analysis and the time lags between latent heating tendency and radial inflow from day 100 to day 120 for Case 1, using the same procedure as in Sect. 4. Just as in our control experiment, we see that the latent heating tendency are negatively correlated with radial inflow. Furthermore, we note that latent heat tendency and cloud fraction possess a positive time-lag with the radial inflow in the outer core

of the TC storm, consistent with the control experiment. This indicates that, statistically, changes in radial inflow *precede* changes in latent heating tendency.

5.2 Results from case 2

Figure 18 shows the radius-height plots of azimuthal velocity and radial velocity within the TCBL for evening (0–6 LST) and afternoon (12–18 LST) from day 100 to day 120 for Case 2. Just as in the control experiment and in Case 1, the radial wind speed shows a clear difference between the evening and afternoon periods. Within the outer core of the TC, there is a statistically significant difference in the radial inflow between the two composites with a deeper and stronger inflow layer in the evening within the outer core of the simulated TC. However, the inflow layer for Case 2 is shallower and weaker than the control experiment and for Case 1. This will have implications for the thermal structure for the TCBL.

Figure 19 shows the radius-height plots of relative humidity, equivalent potential temperature, and virtual potential
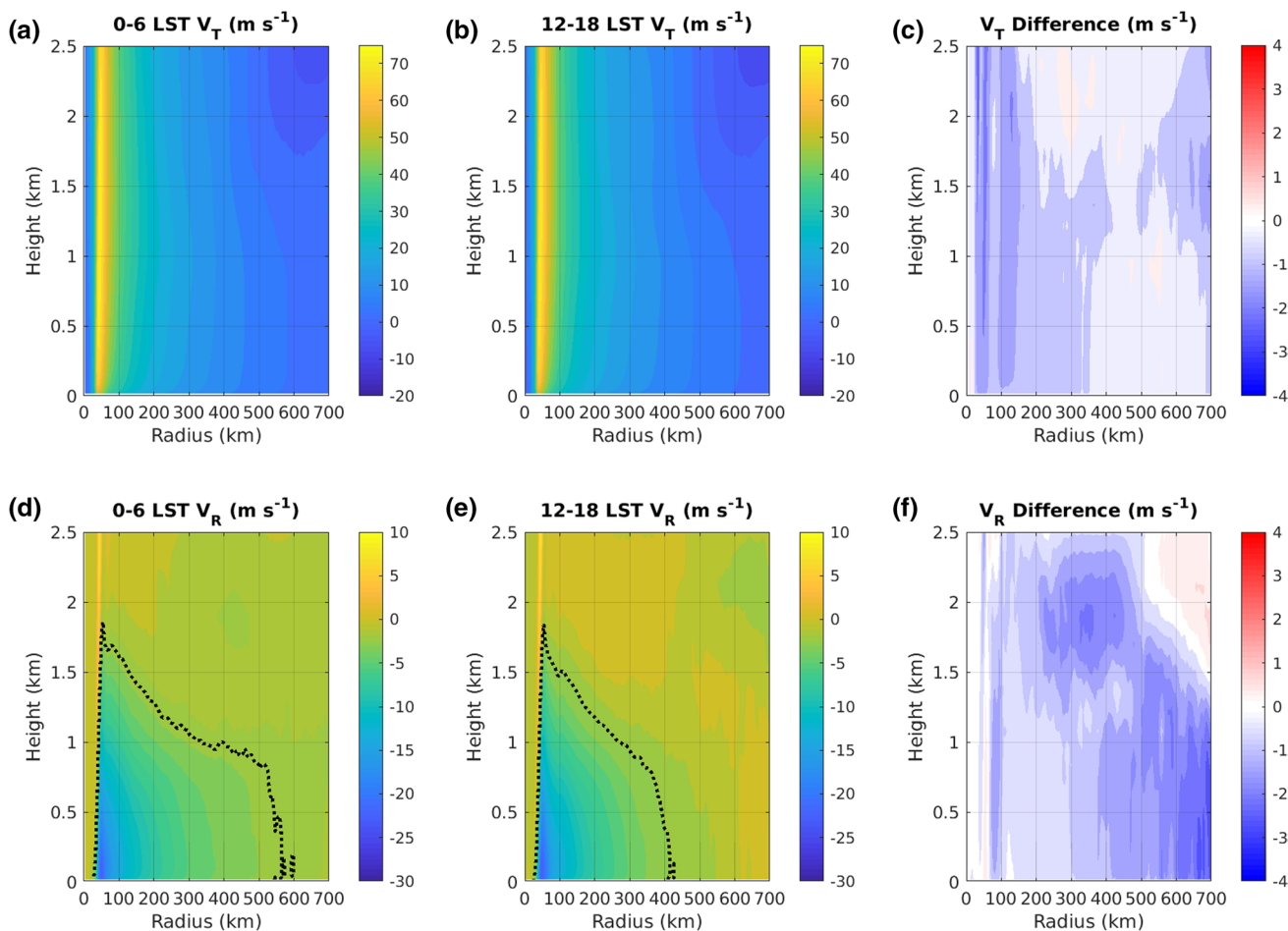
Fig. 18 Same as Fig. 4, except for the simulated storm for Case 2

temperature gradient within the TCBL for evening (0–6 LST) and afternoon (12–18 LST) from day 100 to day 120 for Case 2. Just as in the control experiment and Case 1, the thermal structure of the TCBL for Case 2 possesses a near-surface superadiabatic layer, a mixed layer, and a stable layer. Moreover, we see that θ_e is approximately constant with height within the eyewall and strongly increases towards the eye of the storm with values above 360 K, just as in Case 1. Second, we see that the relative humidity (and thus θ_e) is larger at evening than in the afternoon in the outer core of the TC, consistent with the control experiment and Case 1. However, since the inflow layer is shallower for Case 2 than for the other cases, the diurnal differences in the variables are shifted vertically downward. By comparing Fig. 19 to Fig. 6, we note the diurnal difference in $d\theta_v/dz$ is consistently larger above the inflow layer for Case 2, and the diurnal difference in θ_e is consistently larger in the inflow layer for Case 2.

Figure 20 shows the radius-height plots of temperature tendency due to longwave radiation (LWTEN), temperature tendency due to shortwave radiation (SWTEN), and cloud fraction (CLDFRA) within the TCBL for evening (0–6 LST) and afternoon (12–18 LST) from day 100 to day 120 for Case 2. We note that the cloud fraction and the temperature tendency due to longwave radiation is significantly larger at evening than in the afternoon, whereas the temperature tendency due to shortwave radiation is significantly larger during the afternoon hours. Thus, there is significant longwave cooling at the cloud top in the morning hours and shortwave radiative warming in the evening hours, just as in the control experiment. However, there is significantly less cloud cover for Case 2 than for the control experiment and for Case 1. The decrease in morning cloud cover leads to enhanced shortwave radiative warming and decreased longwave radiative cooling in the morning hours. Furthermore, the overall decreased cloud coverage leads to a smaller diurnal difference in cloud cover for Case 2. A budget analysis of potential temperature (not shown) indicates that the decreased radiative cooling near the cloud top reduces the lapse rate near the cloud base, which tends to make the top of the inflow layer more stable than in the control experiment and Case 1.
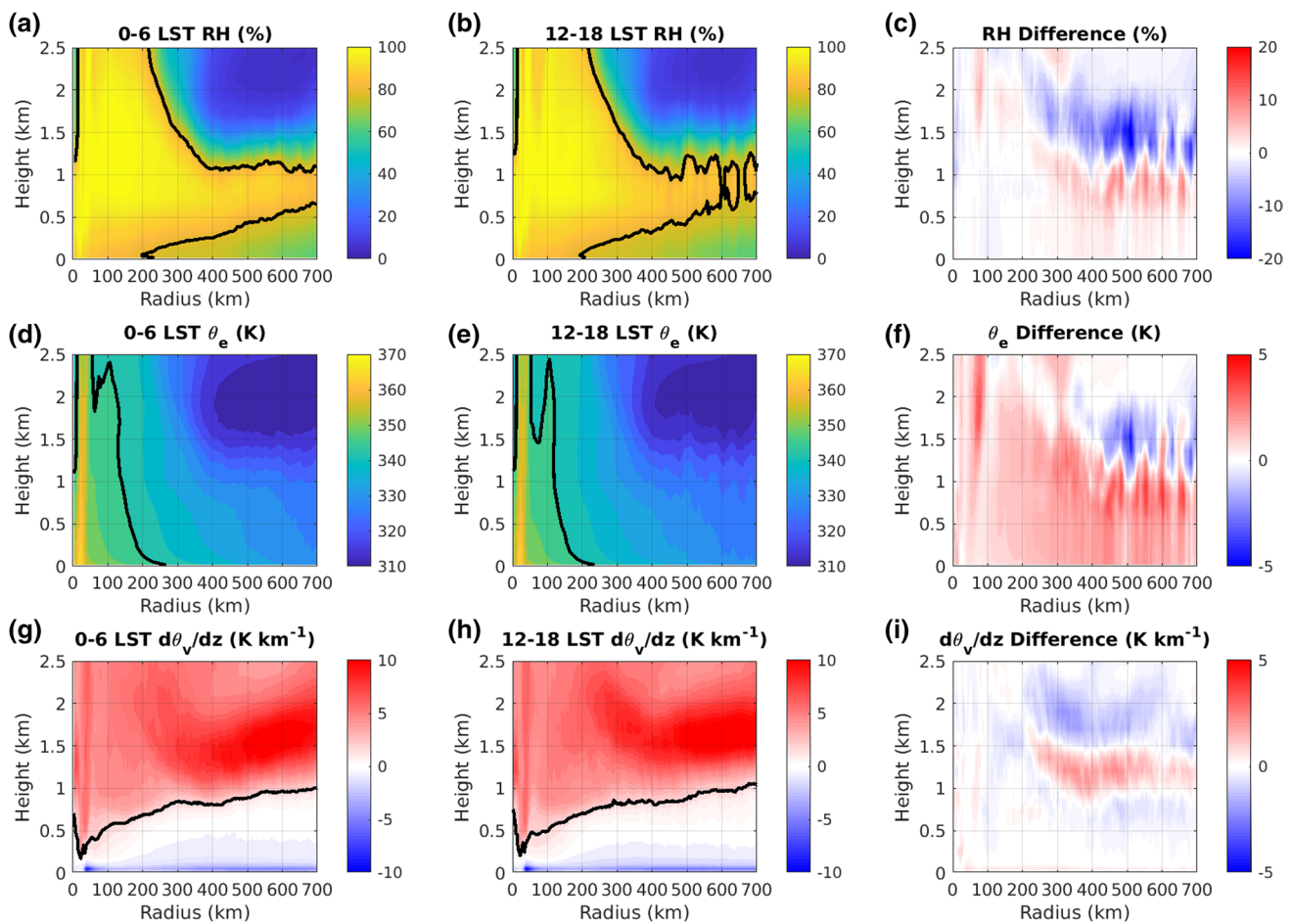
Fig. 19 Same as Fig. 6, except for the simulated storm for Case 2

Table 4 presents the results of the normalized cross-correlation analysis and the time lags between latent heating tendency, cloud fraction, and radial inflow. Just as in our control experiment and in Case 1, we see that the latent heating tendency are negatively correlated with radial inflow. Even though the time-lag has decreased in comparison to Case 1, it still should be noted that there is a positive time-lag between latent heat tendency cloud fraction and cloud fraction with the vertically integrated radial inflow in the outer core of the TC storm.

In conclusion, we note that all major features of the TC diurnal cycle are replicated (including the positive time-lag between radial inflow and latent heating tendency) for Case 1 and Case 2. This indicates that our previous analysis regarding the statistical relationship between convection and radial inflow is not an artifact of the microphysical parameterization or radiation scheme that has been used.

6 Discussion and conclusions

In this study, the diurnal variation of the TCBL has been examined using the non-hydrostatic, axisymmetric cloud model of Bryan and Fritsch (2002). From a statistical cross-correlation analysis, it was found that diurnal changes in radial inflow lag changes in latent heating tendency, which suggests that enhanced radial inflow drives enhanced evening convection within the TCBL. To examine the physical processes that generate the enhanced radial inflow, budget analyses of radial velocity, potential temperature, and water vapor mixing ratio were performed. From the radial velocity budget, it was found that longwave radiative cooling lags the vertical advection of radial velocity, which suggests that the radiational cooling near the cloud base may act to initiate an overturning circulation during the evening hours. Furthermore, as the cooling by longwave radiation diminishes and the warming by shortwave radiation increases, the radial inflow weakens as well. From the potential temperature analysis, it was found that the combined effects of cooling by cloud evaporation and longwave cooling reduces the static
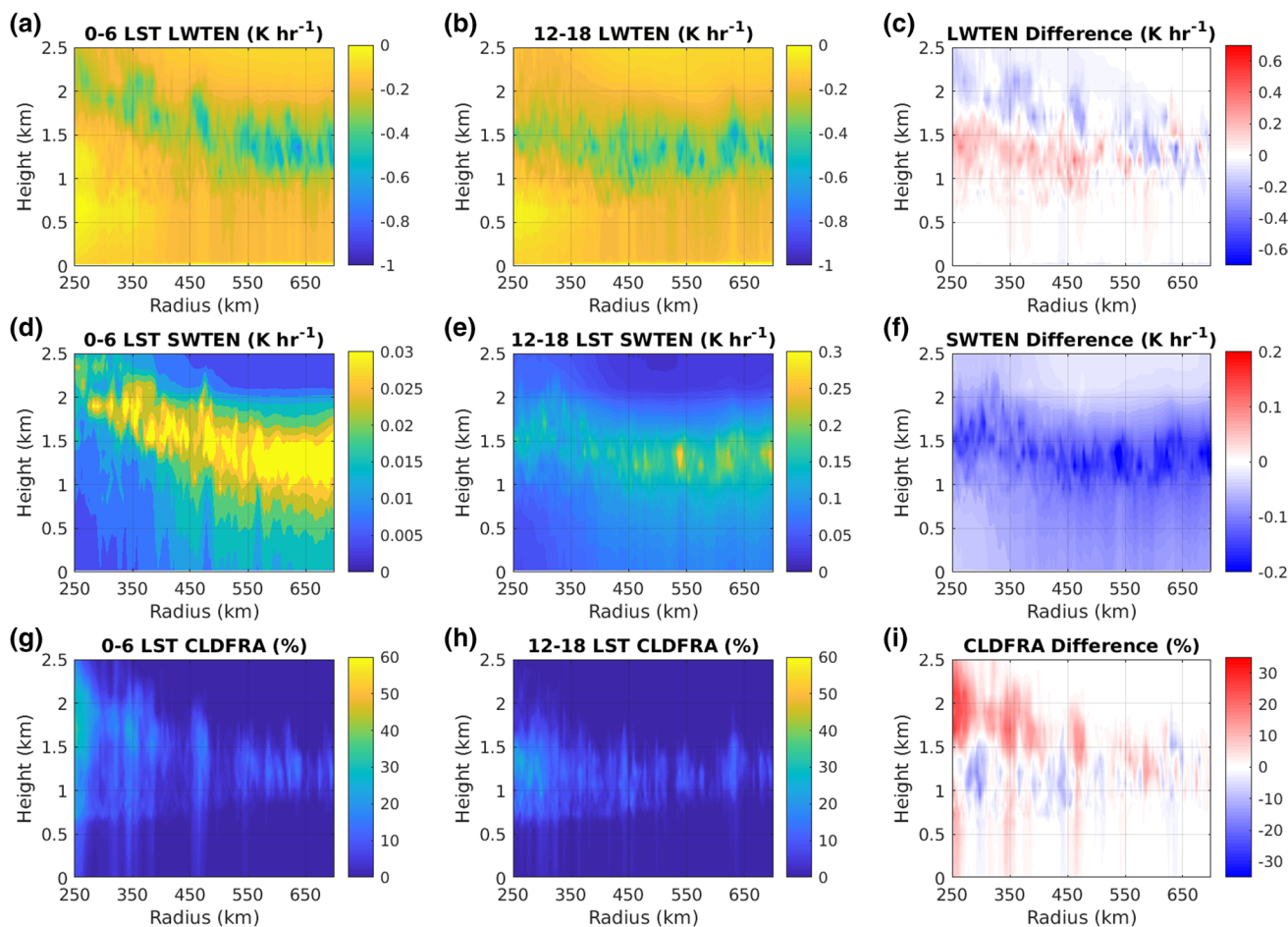
Fig. 20 Same as Fig. 8, except for the simulated storm for Case 2

Table 4 The cross-correlation analysis associated with the inner-core latent heating tendency $\dot{\theta}_{COND,Inner}$, the outer-core latent heating tendency $\dot{\theta}_{COND,Outer}$, and the radial inflow for the simulated TC in Case 2 from day 100 to day 120

Variables	Normalized correlation	Lag (hours)
$\langle \dot{\theta}_{COND,Inner} \rangle, \langle V_R \rangle$	-0.8050	2.0
$\langle \dot{\theta}_{COND,Outer} \rangle, \langle V_R \rangle$	-0.8142	1.0

The variables are defined and calculated in the same manner as discussed in Table 1

stability near the top of the inflow layer, generating convection outside of the inner core of the TC. This suggests that cloud formation within the TCBL induces an anomalous secondary circulation through cloud vs. cloud-free differential heating. From the moisture budget, it was shown that cloud condensation and evaporation processes obtain their maximum amplitude during the evening hours. It was noted that the region of maximum radiational cooling near the cloud base is co-located with the maximum radial moisture advection in this region, and the combined effect of radial and

vertical moisture advection during the evening is to increase relative humidity in the outer regions of the TC near the top of the inflow layer. The idealized simulations illustrate that the relationship between convection and radial inflow during the TCDC, along with the physical processes that govern the enhanced inflow and convection, are not merely artifacts of microphysics parameterizations or radiation schemes.

The model simulations, along with the budget analyses, give a conceptual picture of the physical processes associated with the diurnal variation within the TCBL. The results given here suggests a top-down approach to diurnal variation within the TCBL outside of the inner core. Starting at 12 LST, warming by shortwave radiation near the top of the inflow layer gradually stabilizes the TCBL and increases CIN until sunset. During this time, upward moisture flux continues to moisten the TCBL. At sunset, the warming due to shortwave radiation vanishes, and cloud formation continues. At the cloud base, the cooling due to longwave radiation increases in magnitude, and this gradually weakens CIN through the late evening to early morning hours. In response to this destabilization process, radial outflow is promoted at the cloud base, and

compensating radial inflow and upward vertical motion are generated below the cloud base. For this reason, the strongest updraft in the outer core was generated during 0–6 LST, as shown in Fig. 5. The net effect of this destabilization process is to produce a broader wind field and a stronger secondary circulation, consistent with the results from Bu et al. (2014). The stronger secondary circulation increases surface moisture and enthalpy fluxes, which enhances convection within this region. During sunrise, warming by shortwave radiation diminishes radial inflow at the cloud base, and through a balanced vortex response, the radial inflow weakens.

The results of this study are consistent with the differential radiation mechanism of diurnal circulation adjustment as proposed in Gray and Jacobson (1977) and Ruppert and Hohenegger (2018). According to this hypothesis, the diurnal variation in total radiative heating within an organized convective system (such as the TC inner core) is weak because of the presence of clouds, while in the cloud-free region, subsidence is nocturnally enhanced by strong radiative cooling, and suppressed during the day with reduced cooling. Through mass continuity between the cloud-free and convective regions, ascending motion is enhanced in the convective region at night, and reduced during the day, leading to a nocturnal peak in convective activity. In the current study, it has been shown that the differential radiation pattern created by clouds in the outer core of the TCBL during the evening is virtually reversed during daytime by shortwave heating. In response, this reversal drives changes in circulation as shown in Fig. 5. According to Ruppert and Hohenegger (2018), the differential radiation mechanism delays the nocturnal peak precipitation by about 5 h and is therefore important for heavy precipitation in TCs to peak in early morning.

Based on the simulations presented here, there are additional questions that can be asked to further this study. First, the simulation in this paper assumed a constant sea surface temperature (SST). However, at outer radii from the TC center, it is possible that SST varies diurnally. Future work will examine the role of SST in influencing diurnal variations in TCBL structure. Second, the analysis in this paper primarily addresses the diurnal changes in TCBL structure through a balanced vortex framework. However, previous studies on diurnal transverse circulation show that the unbalanced components of the response may be manifested as outward-propagating gravity waves (Evans and Nolan 2019). Future work will investigate the relationship between TCBL structural changes to unbalanced changes in the middle- and upper-level structure associated with the TCDC.

References

Bell MM, Montgomery MT (2008) Observed structure, evolution, and potential intensity of category 5 Hurricane Isabel (2003) from 12 to 14 September. Mon Weather Rev 136:2023–2046

Bowman KP, Fowler MD (2015) The diurnal cycle of precipitation in tropical cyclones. J Clim 28:5325–5334

Browner SP, Woodley WL, Griffith CG (1977) Diurnal oscillation of cloudiness associated with tropical storms. Mon Weather Rev 136:856–864

Bryan GH, Fritsch JM (2002) A benchmark simulation for moist non-hydrostatic numerical models. Mon Wea Rev 130:2917–2928. https://doi.org/10.1175/1520-0493(2002)130,2917:ABSFMN.2.0.CO;2

Bryan GH, Rotunno R (2009) The maximum intensity of tropical cyclones in axisymmetric numerical model simulations. Mon Wea Rev 137:1770–1789. https://doi.org/10.1175/2008MWR2709.1

Bu YP, Fovell RG, Corbosiero KL (2014) Influence of cloud–radiative forcing on tropical cyclone structure. J Atmos Sci 71:1644–1662. https://doi.org/10.1175/JAS-D-13-0265.1

Chavas DR, Emanuel K (2014) Equilibrium tropical cyclone size in an idealized state of axisymmetric radiative–convective equilibrium. J Atmos Sci 71:1663–1680. https://doi.org/10.1175/JAS-D-13-0155.1

Chou MD, Suarez MJ. (1999) A solar radiation parameterization for atmospheric studies. NASA technical report NASA/TM-1999-10460

Chou MD, Suarez MJ. (2001) A thermal infrared radiation parameterization for atmospheric studies. NASA technical report NASA/TM-2001-104606

Ciesielski PE, Johnson RH, Schubert WH, Ruppert JH (2018) Diurnal cycle of the ITCZ in DYNAMO. J Clim 31:4543–4562. https://doi.org/10.1175/JCLI-D-17-0670.1

Ditchek SD, Corbosiero KL, Fovell RG, Molinari J (2019a) Electrically active tropical cyclone diurnal pulses in the Atlantic basin. Mon Wea Rev 147:3595–3607. https://doi.org/10.1175/MWR-D-19-0129.1

Ditchek SD, Molinari J, Corbosiero KL, Fovell RG (2019b) An objective climatology of tropical cyclone diurnal pulses in the Atlantic basin. Mon Weather Rev 147:591–605. https://doi.org/10.1175/MWR-D-18-0368.1

Donelan MA, Haus BK, Reul N, Plant WJ, Stiassnie M, Graber HC, Brown OB, Saltzman ES (2004) On the limiting aerodynamic roughness of the ocean in very strong winds. Geophys Res Lett 31:L18306. https://doi.org/10.1029/2004GL019460

Drennan WM, Zhang JA, French JR, McCormick C, Black PG (2007) Turbulent fluxes in the hurricane boundary layer part II: latent heat flux. J Atmos Sci 64:1103–1115. https://doi.org/10.1175/JAS3889.1

Dunion JP, Marron CS (2008) A reexamination of the jordan mean tropical sounding based on awareness of the saharan air layer: results from 2002. J Climate 21:5242–5253. https://doi.org/10.1175/2008JCLI1868.1

Dunion JP, Thorncroft CD, Velden CS (2014) The tropical cyclone diurnal cycle of mature hurricanes. Mon Weather Rev 142:3900–3919

Dunion JP, Thorncroft CD, Nolan DS (2019) Tropical cyclone diurnal cycle signals in a hurricane nature run. Mon Weather Rev 147:363–388. https://doi.org/10.1175/MWR-D-18-0130.1

Ebert EE, Curry JA (1992) A parameterization of ice cloud optical properties for climate models. J Geophys Res 97:3831–3836

Evans RC, Nolan DS (2019) Balanced and radiating wave responses to diurnal heating in tropical cyclone-like vortices using a linear nonhydrostatic model. J Atmos Sci 76:2575–2597. https://doi.org/10.1175/JAS-D-18-0361.1

Fairall CW, Bradley EF, Hare JE, Grachev AA (2003) Bulk parameterization of air-sea fluxes: updates and verification for the COARE algorithm. J Climate 16:571–291

Gray WM, Jacobson RW (1977) Diurnal variation of deep cumulus convection. Mon Weather Rev 105:1171–1188

Hawkins HF, Imbembo SM (1976) The structure of a small, intense Hurricane Inez (1966). Mon Weather Rev 104:418–442

Houze RA Jr, Rutledge SA, Matejka TJ, Hobbs PV (1981) The mesoscale and microscale structure and organization of clouds and precipitation in midlatitude clouds. III: Air motions and precipitation growth in a warm-frontal rainband. J Atmos Sci 38:639–649. https://doi.org/10.1175/1520-0469(1981)038%3C0639:TMAMSA%3E2.0.CO;2

Iacono MJ, Delamere JS, Mlawer EJ, Clough SA (2003) Evaluation of upper tropospheric water vapor in the NCAR community climate model (CCM3) using modeled and observed HIRS radiances. J Geophys Res 108:403. https://doi.org/10.1029/2002JD002539

Kepert JD, Wang Y (2001) The dynamics of boundary layer jets within the tropical cyclone core part II: nonlinear enhancement. J Atmos Sci 58:2485–2501

Kepert JD, Schwendike J, Ramsay H (2016) Why is the tropical cyclone boundary layer not "well-mixed"? J Atmos Sci 73:957–973

Knaff JA, Slocum CJ, Musgrave KD (2019) Quantification and exploration of diurnal oscillations in tropical cyclones. Mon Wea Rev 147:2105–2121. https://doi.org/10.1175/MWR-D-18-0379.1

Kossin JP (2002) Daily hurricane variability inferred from GOES infrared imagery. Mon Weather Rev 130:2260–2270. https://doi.org/10.1175/1520-0493(2002)130,2260:DHVIFG.2.0.CO;2

Leppert KD, Cecil DJ (2016) Tropical cyclone diurnal cycle as observed by TRMM. Mon Weather Rev 144:2793–2808

Liu C, Moncrieff MW (1998) A numerical study of the diurnal cycle of tropical oceanic convection. J Atmos Sci 55:2329–2344. https://doi.org/10.1175/1520-0469(1998)055,2329:ANSOTD.2.0.CO;2

Mapes BE, Houze RA Jr (1993) Cloud clusters and superclusters over the oceanic warm pool. Mon Wea Rev 121:1398–1415. https://doi.org/10.1175/1520-0493(1993)121,1398:CCASOT.2.0.CO;2

Mecikalski JR, Tripoli GJ (1998) Inertial available kinetic energy and the dynamics of tropical plume formation. Mon Wea Rev 126:2200–2216. https://doi.org/10.1175/1520-0493(1998)126%3C2200:IAKEAT%3E2.0.CO;2

Melhauser C, Zhang F (2014) Diurnal radiation cycle impact on the pregenesis environment of Hurricane Karl (2010). J Atmos Sci 71:1241–1259

Mlawer EJ, Taubman SJ, Brown PD, Iacono MJ, Clough SA (1997) Radiative transfer for inhomogeneous atmospheres: RRTM, a validated correlated-k model for the longwave. J Geophys Res 102:16663–16682

Montgomery MT, Zhang JA, Smith RK (2014) An analysis of the observed low-level structure of rapidly intensifying and mature hurricane Earl (2010). Q J R Meteorol Soc 140:2132–2146

Morrison H, Thompson G, Tararskii V (2009) Impact of cloud microphysics on the development of trailing stratiform precipitation in a simulated squall line: comparison of one- and two-moment parameterizations. Mon Wea Rev 137:991–1007

Muramatsu T (1983) Diurnal variations of satellite-measured TBB areal distribution and eye diameter of mature typhoons. J Meteor Soc Japan 61:77–90. https://doi.org/10.2151/jmsj1965.61.1_77

Navarro EL, Hakim GJ (2016) Idealized numerical modeling of the diurnal cycle of tropical cyclones. J Atmos Sci 73:4189–4201. https://doi.org/10.1175/JAS-D-15-0349.1

Navarro EL, Hakim GJ, Willoughby HE (2017) Balanced response of an axisymmetric tropical cyclone to periodic diurnal heating. J Atmos Sci 74:3325–3333. https://doi.org/10.1175/JAS-D-16-0279.1

O'Neill ME, Perez-Betancourt D, Wing AA (2017) Accessible environments for diurnal-period waves in simulated tropical cyclones. J Atmos Sci 74:2489–2502. https://doi.org/10.1175/JAS-D-16-0294.1

Pfister L, Chan KR, Bui TP, Bowen S, Legg M, Gary B, Kelly K, Proffitt M, Starr W (1993) Gravity waves generated by a tropical cyclone during the STEP tropical field program: A case study. J Geophys Res 98:8611–8638. https://doi.org/10.1029/92JD01679

Randall DA, Harshvardhan R, Dazlich DA (1991) Diurnal variability of the hydrologic cycle in a general circulation model. J Atmos Sci 48:40–62. https://doi.org/10.1175/1520-0469(1991)048%3c0040:DVOTHC%3e2.0.CO;2

Rotunno R, Emanuel KA (1987) An air–sea interaction theory for tropical cyclones part II: evolutionary study using a nonhydrostatic axisymmetric numerical model. J Atmos Sci 44:542–561

Ruppert JH, Hohenegger C (2018) Diurnal circulation adjustment and organized deep convection. J Climate 31:4899–4916. https://doi.org/10.1175/JCLI-D-17-0693.1

Ruppert JH, O'Neill ME (2019) Diurnal cloud and circulation changes in simulated tropical cyclones. Geo Res Let 46:502–511. https://doi.org/10.1029/2018GL081302

Tang X, Zhang F (2016) Impacts of the diurnal radiation cycle on the formation, intensity, and structure of Hurricane Edouard (2014). J Atmos Sci 73:2871–2892. https://doi.org/10.1175/JAS-D-15-0283.1

Thompson G, Field PR, Rasmussen RM, Hall WD (2008) Explicit forecasts of winter precipitation using an improved bulk microphysics scheme part II: implementation of a new snow parameterization. Mon Wea Rev 136:5095–5115

Tripoli GJ, Cotton WR (1989) Numerical study of an observed orogenic mesoscale convective system. Part I: Simulated genesis and comparison with observations. Mon Wea Rev 117:273–304. https://doi.org/10.1175/1520-0493(1989)117%3C0305:NSOAOO%3E2.0.CO;2

Weickmann HK, Long AB, Hoxit LR (1977) Some examples of rapidly growing oceanic cumulonimbus clouds. Mon Wea Rev 105:469–476. https://doi.org/10.1175/1520-0493(1977)105,0469:SEORGO.2.0.CO;2

Williams GJ Jr (2016) The inner core thermodynamics of the tropical cyclone boundary layer. Meteorol Atmos Phys. https://doi.org/10.1007/s00703-016-0441-5

Williams GJ Jr (2019) The effects of ice microphysics on the inner core thermal structure of the hurricane boundary layer. Meteorol Atmos Phys 131:987–1003. https://doi.org/10.1007/s00703-018-0616-3

Willoughby HE (1998) Tropical cyclone eye thermodynamics. Mon Wea Rev 126:3053–3067. https://doi.org/10.1175/1520-0493(1998)126%3C3053:TCET%3E2.0.CO;2

Wu Q, Ruan Z (2016) Diurnal variations of the areas and temperatures in tropical cyclone clouds. Quart J Royal Meteorol Soc 142:2788–3279. https://doi.org/10.1002/qj.2868

Yang G, Slingo J (2001) The diurnal cycle in the tropics. Mon Wea Rev 129:784–801. https://doi.org/10.1175/1520-0493(2001)129,0784:TDCITT.2.0.CO;2

Zhang JA, Rogers RF, Nolan DS, Marks J, Frank D (2011) On the characteristic height scales of the hurricane boundary layer. Mon Wea Rev 139:2523–2535. https://doi.org/10.1175/MWR-D-10-05017.1

Zhang JA, Dunion JP, Nolan DS (2020) In situ observations of the diurnal variation in the boundary layer of mature hurricanes. Geo Res Let. https://doi.org/10.1029/2019GL086206